GESP-589
NASA-CR-72830

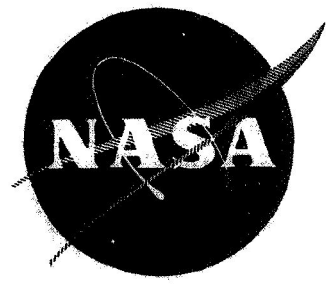

TOPICAL REPORT NO. 5
SNAP-8 REFRACTORY BOILER DEVELOPMENT PROGRAM

SHELL SIDE HYDRAULIC CHARACTERISTICS OF A FULL-SCALE SNAP-8 MULTIPLE TUBE MODEL BOILER

By
E. S. Hsia
R. A. Fuller

prepared for
NATIONAL AERONAUTICS AND SPACE ADMINISTRATION

NASA Lewis Research Center
Contract NAS 3-10610
Edward R. Furman, Project Manager

NUCLEAR SYSTEMS PROGRAMS
SPACE SYSTEMS
GENERAL ELECTRIC
CINCINNATI, OHIO 45215

Requests for copies of this report should be referred to:

National Aeronautics and Space Administration
Scientific and Technical Information Division
Attention: USS-A
Washington, D.C. 20546

GESP-589

TOPICAL REPORT NO. 5

SNAP-8 REFRACTORY BOILER DEVELOPMENT PROGRAM

SHELL SIDE HYDRAULIC CHARACTERISTICS OF A FULL-SCALE SNAP-8 MULTIPLE TUBE MODEL BOILER

prepared by

E. S. Hsia
R. A. Fuller

NUCLEAR SYSTEMS PROGRAMS
SPACE DIVISION
GENERAL ELECTRIC COMPANY
Cincinnati, Ohio 45215

prepared for

NATIONAL AERONAUTICS AND SPACE ADMINISTRATION

NASA Lewis Research Center
Contract NAS 3-10610
Edward R. Furman, Project Manager

FOREWORD

The work described in this report is part of the SNAP-8 Refractory Metal Boiler Development Program, NASA Contract NAS 3-10610, conducted by the General Electric Company. The work was done under the technical management of R. D. Brooks of the General Electric Company and E. R. Furman of the Lewis Research Center, NASA.

ABSTRACT

Shell side hydraulic characteristics of a full-scale SNAP-8 multiple-tube model boiler were thoroughly investigated over a turbulent Reynolds number range from 18,000 to 38,000. Friction factors for flow parallel to a tube bundle with or without turbulence promoters have been determined experimentally. Loss coefficients for tube supporting spacers and exit or inlet manifolds were also measured experimentally. In addition, the effect of the incoming flow condition on these loss coefficients was investigated. With the aid of upstream dye injections, a visual study was made on the shell side flow distribution affected by turbulence promoters and the exit hole-slotted baffle. Results are presented in graphical forms.

TABLE OF CONTENTS

LIST OF FIGURES

NOMENCLATURE

SYMBOLS	DESCRIPTION	DIMENSIONS
A_F	Net Flow Area	in^2
c	Clearance Between the Shell I.D. and Bundle Diameter	inch
C	Constant used in Equation (13)	dimensionless
d_w	Wire Coil Diameter	inch
D	Diameter	inch
D_e	Equivalent Diameter Defined by Equation (4)	inch
D_s	Shell Inside Diameter	inch
f	Friction Factor	dimensionless
g	Gravitational Acceleration	ft/sec^2
H_v	Velocity Head	psi
ΔH	Measured Manometer Height	inch
K	Loss Coefficient	dimensionless
K*	Loss Coefficient Based Upon Shell Side Velocity Head	dimensionless
L	Tube Length	inch
P_w	Wire Coil Pitch	inch
ΔP	Measured Pressure Drop	psi
N_{Re}	Reynolds Number, $\frac{\rho D_e V}{\mu}$	dimensionless
V	Shell Side Average Velocity	ft/sec
W_{H_2O}	Water Flow Rate	lb/sec
ρ	Density	lb/ft^3
μ	Absolute Viscosity	lb/Hr-ft
γ_m	Specific Gravity for Meriam	dimensionless
ϵ	Absolute Roughness	inch
ϕ	Mixing Parameter Defined by Equation (9)	dimensionless

Subscripts

ax	Axial Flow
eh	Exit Radial Ports
em	Exit Manifold
sh	Shell Side
sp	Spacer
wc	Wire Coil

I INTRODUCTION

Shell side flow frictional characteristics and flow distribution play an important part in the shell and tube heat exchanger design. Pressure losses, fluid-flow distribution and fluid-flow mixing are often determining factors in the design of a reliable, high performance heat exchanger. However, many aspects of the problems associated with the shell side fluid-flow are very difficult to treat analytically and recourse to experimental results obtained from model tests by using water or other easy fluid as the working fluid will be useful and necessary.

In most heat exchangers, turbulent flow outside of and parallel to the axis of a tube bundle is of frequent occurrence and pressure drop data specifically applicable to a particular geometry are not generally available in the literature. Furthermore, the calculation or prediction of the shell side fluid-flow frictional characteristics when the fluid flows across tube supporting spacers, turbulence promoters, and exit or inlet flow distribution devices are complicated by the fact that there is no way analytically to predict their loss coefficients. For this reason, model tests are also necessary in order to secure a dependable heat exchanger design.

A series of shell side flow hydraulic tests of a model boiler by using water as the working fluid were conducted by Nuclear Systems Programs, General Electric Company for NASA under contract NAS 3-10610, SNAP-8 Refractory Boiler Development Program, to evaluate the frictional characteristics of the full-scale SNAP-8 refractory metal boiler. A geometrically full-scale simulated model boiler was used in the test. Figure (31) gives a photographic view of such a shell and tube model

boiler assembly. A detailed description of the test section will be given subsequently in Section II.

Nine combinations of wire coil (wire diameter x pitch) were employed in the present test for flow distribution studies. The wire coils were used as turbulence promoters by wrapping them around the tube bundle. Three different geometries of tube supporting spacers were tested for evaluating the individual loss coefficient. A plexiglass model of the exit or inlet manifold and flow baffle assembly which was designed to insure uniform flow distribution in the exit or inlet region was also tested to evaluate its performance. The detail design approach of such an assembly was given in Reference (1).

Measurement of the following pressure losses were accomplished in the present study:

(1) Shell side axial flow passing the tube bundle.

(2) Shell side perturbed axial flow (by helically wrapped wire coil around the tube bundle) passing the tube bundle.

(3) Tube supporting spacers with three different geometries, subject to incoming axial flow or perturbed axial flow.

(4) Exit or inlet manifold.

In general, frictional losses are calculated as recommended by McAdams [2] by calculating a hydraulic equivalent diameter for the tube bundle and subsequently using it as a round tube diameter in a conventional frictional factor correlation equation. Therefore, a comparison was then made between the present test data and the conventional pressure loss prediction for the axial flow case to see whether frictional losses calculated by the conventional methods were sufficiently accurate for design uses.

Sufficient pressure loss test data were accumulated and correlated over the turbulent Reynolds number range of $1.8 \times 10^4 \leq N_{Re} \leq 3.8 \times 10^4$. For the purpose of future design uses, the conventional friction factors and loss coefficients were evaluated from test data for axial flow, perturbed axial flow, spacers and exit or inlet manifolds. The results are presented in graphical form.

II DESCRIPTION OF TEST APPARATUS

A schematic of the test setup and the test section used to conduct the shell side flow study are shown in Figures (1) and (2) respectively. As shown in Figure (1), plant water at a maximum pressure of 50 psia is first passed through a standard 2.1-inch orifice to measure the flow rate. The water flow rate was controlled by a manually operated control valve and was measured by reading the pressure drop across the orifice plate with a mercury manometer. The orifice calibration curve is given in Figure (7). The water then flows through a 2 1/2-inch fire hose and comes to the transparent model boiler shell test section, where all six pressure loss measurements were taken. After running through the boiler shell and exit manifold assembly, the running water was discharged into a drain after passing through a 2 1/2-inch, 30-foot long fire hose.

As shown in detailed dimensions in Figure (3), the tube bundle consists of seven stainless steel oval-shaped tubes. The equilateral triangular-pitched tube bundle used in the present test closely resembles the one actually employed in the SNAP-8 power conversion system. The 21-foot long tube bundle was then fitted snugly into the 20-foot long, 4.75-inch ID model boiler shell which is made of transparent plexiglass for the purpose of flow visualization. Finally the model boiler shell test section was installed in the hydraulic test stand as shown in Figure (1).

The exit manifold assembly which is shown in detail in Figures (2) and (4), was then connected to the boiler shell at the exit end. The specially designed exit or inlet manifold assembly featured a series of different sized radial ports on the shell wall. These radial ports were so sized to insure a uniform radial flow distribution in the flow exit region[1].

Copper wire coil with various combinations of sizes and pitches was used over a 5-foot axial tube length as a turbulence promoter for the shell side fluid-flow by wrapping it around the tube bundle. Tests were conducted in this perturbed axial flow region according to the following test plan matrix:

Wire Size	Wrapped Pitch			
1/8" D	3"	-	-	-
3/16" D	3"	6"	10"	20"
1/4" D	3"	6"	10"	20"

Two tube supporting spacers with exactly the same shapes were placed in test sections II and IV. The purpose of this arrangement is to study the frictional characteristics of shell side fluid-flow passing the same spacer but with different incoming flow conditions, i.e., pure incoming axial flow for test section II and perturbed axial flow for test section IV. Three different designs of spacer geometry were used in the test. As shown in Figure (5), the spacer under the name "Rod Spacer" was the one currently used in Boiler SN-1 which was under endurance test at Nuclear Systems Programs, General Electric Company, since February, 1967 and the one under the name of "Spacer No. 2" was the revised version of "Spacer No. 1" which was originally designed for the redesigned SNAP-8 boiler.

Listed below are the six test section pressure loss measurements as shown in Figure (2). They are designated as follows:

$(\Delta P)_I$ Pressure loss for axial flow parallel to the tube bundle over 5-foot axial tube length.

$(\Delta P)_{II}$ Pressure loss for the spacer subject to incoming axial flow.

$(\triangle P)_{III}$ Pressure loss for the helical wire coil region over 5-foot axial tube length.

$(\triangle P)_{IV}$ Pressure loss for the spacer subject to incoming perturbed axial flow.

$(\triangle P)_{V}$ Pressure loss for fluid-flow across the shell tube radial ports.

$(\triangle P)_{VI}$ Pressure loss for fluid-flow across the circular exit manifold.

Static pressure tap holes, suitably located for measuring individual pressure drop for shell side fluid-flow across the entire boiler assembly were provided in each of the above mentioned test sections. For the purpose of obtaining accurate and reliable pressure drop data, an effort was made to use a piezometer ring on each pressure tap location, that is, an interconnected set of static pressure holes (eight holes had been used in each location) around the perimeter of the boiler shell in a plane normal to the direction of fluid-flow.

Six standard 30-inch manometers, made by ther Meriam Instrument Co., were used to measure the pressure differential across each test section. The indicating fluid is Meriam D-8325 which has a specific gravity of 1.745 at 60°F. The manometers are subdivided into 1/10-inch.

Two dye injections located three feet upstream from test section I were employed for the photographic recording and visual observation of the flow distribution in the wire coil and exit manifold regions. A hypodermic (needle and syringe) was used to inject dye into the stream at a sufficient rate to insure adequate color. A tank of compressed argon gas was used to supply the back pressure for the hypodermic.

III DESCRIPTION OF TESTING PROCEDURES

The detailed operating procedures for the present shell side model boiler hydraulic test are listed successively as follows:

A. Initial Startup

Step (1) Open water control valve
Allow water to pass through the test section and gradually fill the test section.

Step (2) Check and eliminate air bubbles entrapped along all pressure lines.

B. Pressure Readings

Step (1) Set up desired flow rate by controlling the water valve manually.

Step (2) Pressure reading at the orifice.

Step (3) Pressure reading at each test section.

Step (4) Set up higher flow rate by operating the water control valve.

Step (5) Repeat steps (2), (3) and (4) until the maximum allowable water flow rate is reached.

C. Dye Injection

Step (1) Set up photographic equipment if picture is required to be taken at some particular section along the model boiler.

Step (2) Fill enough dye into the hypodermic and open the dye control valve.

Step (3) Observe and record the flow distribution as the dye flows and mixes with the shell side water flow in the wire coil region and exit manifold region.

Step (4) Picture taken if required.

Step (5) Repeat steps (2) and (3) if necessary.

D. Temperature Reading

Step (1) Periodically take the temperature reading of the running water at the exit section by using a thermometer.

E. Change of Spacers and Wire Coil

Step (1) Close water control valve and let water drain gradually from the test section.

Step (2) Disconnect the exit manifold assembly.

Step (3) Pull out the tube bundle.

Step (4) Install the new wire coil combination (wire diameter x pitch) and the spacer.

Step (5) Fit the tube bundle into the boiler shell and connect the exit manifold assembly.

Step (6) Repeat steps in (A), (B), (C) and (D).

The following general rules were constantly exercised in taking all the pressure drop readings:

(1) Allow a reasonable period of time for the system to reach a steady state condition before pressure readings were taken.

(2) During the test, water flow rates were raised gradually from the initial start-up value up to its maximum allowable value. For each run a repeatability check of the test data was performed by reducing the flow rate from its maximum value back to some intermediate value.

(3) Special attention was taken before all pressure readings to insure that all pressure lines were free from entrapped air bubbles.

(4) The Meriam manometers were all cleaned and refilled with the fresh indicating fluid before the test took place. In addition, for each test run all the manometers were carefully checked to avoid errors due to impurities in the measuring system or faulty readings.

(5) Special care was taken for wrapping the wire coil around the tube bundle to insure evenly wrapped pitch and no compression on the tube bundle assembly.

(6) Attention was constantly taken to check any leakage at connections, fittings and glued parts.

IV DATA REDUCTION AND PRESSURE LOSS CORRELATION

A. Data Reduction Procedures

(1) Water Flow Rate W_{H_2O} (lb/sec)

During the test, the water flow rate was measured by the pressure differential across the 2.1-inch orifice plate from a mercury manometer in units of inches of mercury. A calibration curve, as shown in Figure (7), was then used to obtain the water flow in lb/sec.

(2) Pressure Loss, ΔP (psi)

All pressure loss readings along the model boiler test section were recorded in units of inches of Meriam fluid. The specific gravity of such indicating fluid was furnished by the maker, the Meriam Instrument Co. and given in Figure (6). The pressure loss in psi is then calculated by the following equation

$$\Delta P = 62.4\ (\gamma_m - 1)\ (\Delta H)\ \frac{1}{1728} = 0.0271\ (\Delta H) \qquad (1)$$

Where $\gamma_m = 1.75$, the specific gravity for Meriam fluid at 60°F, was used. ΔH, expressed in inches, denotes the height differential from the Meriam manometer readings.

(3) Friction Factor, f

In the pipe flow, it has been found convenient to correlate the pressure loss under turbulent flow conditions in terms of the velocity head, $\frac{\rho V^2}{2g}$, the friction factor, f, and the passage length to diameter ratio, $\frac{L}{D}$. Thus the pressure loss

is expressed as,

$$\Delta P = f \left(\frac{\rho V^2}{2g}\right) \left(\frac{L}{D}\right)$$

or $$f = \frac{\Delta P}{\left(\frac{L}{D}\right) H_v} \qquad (2)$$

Equation (2) applies to the flow through circular passages, However, it has been found that the same turbulence intensity and the same friction factor correlation prevail if the ratio of the flow passage area to the wetted perimeter is kept constant. This ratio is called the hydraulic radius and 4 x (hydraulic radius) is defined as the hydraulic equivalent diameter, D_e. Therefore, Equation (2) can be extended to correlate the pressure loss for fluid-flow passing through passages other than the circular pipe if the hydraulic equivalent diameter concept is used. Thus we have,

$$f = \frac{(\Delta P)_{measured}}{\left(\frac{L}{D_e}\right) (H_v)_{sh}} \qquad (3)$$

Where D_e is calculated by the following relation,

$$D_e = 4 \left(\frac{\text{Shell side net flow area}}{\text{Shell side wetted perimeter}}\right) \qquad (4)$$

and $(H_v)_{sh}$ which denotes the shell side velocity head has the the following expression,

$$(H_v)_{sh} = \frac{\rho V^2_{sh}}{2g} = \frac{1}{2g\rho} \left(\frac{W_{H_2O}}{A_F}\right)^2 \qquad (5)$$

With A_F denoting the shell side net flow area.

(4) Loss Coefficient, K

In a conventional way, the fluid flow pressure loss caused by passing obstacles, changes in passage directions, changes in passage cross-sections, etc., can be correlated by multiplying some appropriate velocity heads by a loss coefficient, that is

$$\Delta P = K\left(\frac{\rho V^2}{2g}\right) \tag{6}$$

or

$$K = \frac{(\Delta P)_{measured}}{H_v}$$

(5) Reynolds Number, N_{Re}

Reynolds number in the present test was based upon the shell side average velocity and the hydraulic equivalent diameter D_e, defined in Equation (4). We have,

$$N_{Re} = \frac{\rho D_e V}{\mu} = \frac{D_e}{\mu}\left(\frac{W_{H_2O}}{A_F}\right) \tag{7}$$

Where the absolute viscosity, μ, for water was evaluated according to the temperature of the running water at the exit of the test section. Since there is no heat transfer involved in the present hydraulic test, it is believed that all tests were made under approximately isothermal conditions.

B. Pressure Loss Correlations

(1) Axial Flow Passing Tube Bundle

Almost fifty pressure drop data points were accumulated for test section I, i.e., axial shell side flow passing through the tube bundle over a 5-foot tube length. The pressure loss and friction factor calculated by Equations (1) and (3) are presented in Figures (8) and (9). A comparison was made between the present measured data and the value predicted by the conventional pressure loss correlation. The Blasius friction factor equation

is used for the comparison and has the following expression,

$$f = 0.316 \, (N_{Re})^{-1/4} \qquad (8)$$

for smooth pipes with N_{Re} ranging from 3,000 to 100,000.

As shown in Figure (9), it is noted that the experimental friction factor from the present test is about 10 to 20% lower than the value predicted by the conventionally used formula in Equation (8).

(2) Perturbed Axial Flow Passing Through Wire Coil Wrapped Tube Bundle

Nine wire coil combinations (wire diameter x pitch) were tested over a Reynolds number range of $1.8 \times 10^4 \leq N_{Re} \leq 3.8 \times 10^4$. Pressure loss data calculated from Equation (1) was presented in Figure (10). Plots of the ratio $\frac{(\triangle P)_{wc}}{(\triangle P)_{ax}}$, i.e., the pressure loss ratio of the perturbed axial flow to the axial flow over the same 5-foot tube length at the same Reynolds Number, are presented in Figures (11) to (13) for various wire coil combinations. As shown by these figures, the general trend of pressure losses was found to be directly proportional to the wire size and inversely proportional to the wire pitch. For the purpose of comparing the turbulent or mixing level induced by the various wire coil combinations, a mixing parameter ϕ is introduced and defined as follows,

$$\phi = \sqrt{1 + \left(\frac{\pi D_s}{P_w}\right)^2 \left(\frac{d_w}{c}\right)^2} \qquad (9)$$

Where $\left(\frac{P_w}{D_s}\right)$ is the ratio of wire pitch to the shell inside diameter and $\left(\frac{d_w}{c}\right)$ is the ratio of the wire diameter to the clearance between the shell inside diameter and the tube bundle diameter.

The following table shows the turbulence level in terms of ϕ defined above for various wire coils tested. Also, shown in this table, are the distances required for developing a fully mixed flow region. These distances were visually determined by upstream dye injections.

Mixing Parameter ϕ	Wire Coil Combination (wire dia. x pitch)	Distance Required for Developing a Fully Mixed Region*
3.93	1/4" x 3"	6"
2.22	3/16" x 3"	10"
2.08	1/4" x 6"	12"
1.41	1/4" x 10"	15"
1.18	3/16" x 6"	15"
0.985	1/4" x 20"	20"
0.96	1/8" x 3"	45"
0.795	3/16" x 10"	20"
0.58	3/16" x 20"	30"

* Distance Measured from the start of the wire coil region.

Friction factors for fluid flow passing through the wire coil region were calculated by Equation (3) and the results were presented in Figures (14) to (16) for various turbulence levels induced by the wire coil. These figures show that the friction factors are not too much dependent upon the Reynolds number.

Several interesting plots in Figures (17) and (18) show the effect of the wire size, wire pitch and turbulence on the frictional characteristic for the axially perturbed flow passing the tube bundle. After digesting these plots, a compromise seems to exist between pressure loss and turbulence before selecting the best wire coil combination for the design purpose.

(3) Spacer Subject to Incoming Axial or Perturbed Axial Flow

As described before, two spacers with exactly the same geometry were installed in test sections II and IV for evaluating the loss coefficient under different incoming flow conditions. In test

section II, the incoming flow is purely axial and in test section IV, the incoming flow is perturbed or distorted from the axial flow condition by installing a helical wire coil in the upstream. Effort was made in the present test to evaluate the influence of different incoming flow conditions on frictional characteristics when shell side flow passes through tube supporting spacers.

Three sets of spacers with different geometries, as illustrated in Figure (5) were tested. Figure (19) shows the pressure loss for these three differently designed spacers when the incoming flow was axial only. As the figure shows, the SN-1 Boiler Rod spacers has the greatest pressure drop over spacers No. 1 and No. 2. In addition, the pressure drop for spacer No. 2 is about 30 - 40% of that value for Spacer No. 1. The tested spacers No. 1 and No. 2 were recently designed for the SNAP-8 new boiler assembly, and as manifested by the present test results, the pressure loss reduction for spacer No. 2 is valuable for the final selection of tube supporting spacers. The design consideration is even more severe in the case where a large number of spacers are required for a long boiler, and the overall shell side allowable maximum pressure loss is limited.

The effects of upstream distorted flow on the pressure loss for various spacers are presented in Figure (21). The distorted level of the incoming flow is indicated by the mixing parameter ϕ defined previously. As we can see from this figure, the pressure loss across the spacer is directly proportional to the incoming flow distorted levels. For example, in the rod spacer case with $\phi = 3.92$ (1/4-inch x 3-inch wire coil in the upstream) the pressure drop is about 1.2 times greater than the case with $\phi = 0$ (no wire coil in the upstream). However, as shown in Figures (22) and (23) the effect of upstream turbulence level is generally small on the frictional characteristics when fluid flow passes through the spacers. In the range of the wire coil used in the present test, the deviations in pressure loss are generally less than 20% off from the axial flow values.

For the purpose of practical design uses, loss coefficients for various spacers were calculated from Equation (6) based upon the velocity head through the spacer. The results are presented in Figures (20), (22) and (23) over the Reynolds number range of $1.8 \times 10^4 \leq N_{Re} \leq 3.8 \times 10^4$. These figures show that the spacers' loss coefficients are almost independent of Reynolds numbers.

(4) Fluid Flow Through Shell Radial Ports and Exit Manifold

As illustrated in Figure (4), the shell side flow path in the exit region is featured by a sudden turn from its axial direction to the circular path in the manifold by passing through a series of different sized radial holes on the shell wall. In the present test, pressure losses were measured for the flow passing these holes and the circular manifold separately. About fifty data points were accumulated and their average values were presented in Figure (24). It can be readily concluded from this figure that the pressure loss across the radial hole is about 85 - 90% of the total pressure drop for the whole exit assembly.

Loss coefficients for radial holes and circular manifold, K_{eh} and K_{em}, respectively were calculated from Equation (6) and presented in Figure (25). The velocity heads used in the calculation were evaluated based upon the flow area through radial holes and manifold, respectively. In addition, one more effort was made to examine the upstream distorted flow effect on the exit region. As shown in Figure (26), it is noted that there is no appreciable effect from upstream turbulence on the exit region pressure loss over the size of the turbulence promoter being employed in the present test.

V VISUAL STUDIES OF FLOW DISTRIBUTION

Visual and photographic observations of the shell side flow mixing phenomena were simultaneously made with the static pressure drop measurements. Of particular interest was the shell side flow mixing produced by adding turbulence promoters and the flow distribution at the exit region.

A. Shell Side Flow Distribution and Mixing in the Exit Region

A plexiglass model of the exit manifold and flow baffle assembly which was designed to insure uniform flow distribution in the exit region was employed for visual study of the nature of shell side flow in this end region. As illustrated in Figures (34)and (34a), an earlier picture which was taken without installing the exit manifold assembly showed very bad flow distribution in the exit region. However, after installing the exit manifold assembly, the picture was quite changed from the one shown in Figure (34). As shown in Figures (35) and (35a), the shell side flow first comes in axially and then undergoes a 90° turn through a series of various-sized holes on the shell tube. These radial holes were so sized as to meet the condition of uniform flow distribution[1]. Similar good mixing and flow distribution resulted when a turbulence promoter of 1/4-inch x 6-inch wire coil was installed in the upstream.

B. Mixing of Shell Side Flow as Effected by Turbulence Promoters

As described before, nine wire coil combinations (wire diameter x pitch) were used as turbulence promoters by wrapping the wire coil

around the tube bundle. Upstream dye injections were used for visualization of the shell side flow mixing phenomena. As illustrated in Figures (36) and (36a), dye was injected at two upstream locations (180° apart) and the shell side flow had indicated no mixing at all without wrapping the wire coil around the tube bundle. On the contrary, as shown in Figures (37) and (37a), the shell side flow did show very good mixing after wrapping a wire coil (3/16-inch x 3-inch) around the tube bundle. Both pictures, as illustrated in Figures (36) and (37), were taken at a distance of about six feet downstream from the dye locations.

The mixing effect of various turbulence promoters was then evaluated by observing the turbulent level of shell side flow with the aid of dye injections. Furthermore, the distances required for developing a fully mixed region were also visually determined for various wire coil combinations. These entrance lengths were listed in the table shown in Section IV. In general, all the wire coil combinations except the one with the combination of 1/8-inch x 3-inch indicate good mixing of the shell side flow after their entrance lengths. The wire coil of 1/8-inch x 3-inch combination was found to require an unreasonably long entrance length of 45 inches and even after this entrance length, the mixing was still poor as compared with the results produced by the rest of the wire combinations. The entrance length for the wire coil combinations of 3/16-inch x 6-inch is qualitatively shown in Figure (37a).

The present visual and photographic study of the shell side flow mixing by employing turbulence promoters leads to the following conclusions:

(1) Shell side flow mixing is found to be directly proportional to the wire coil diameter and inversely proportional to the

wrapping pitch.

(2) A 1/8-inch wire with tight pitch of 3-inches was found very poor with respect to the mixing effect. The clearance, C, defined as the distance between the shell inside diameter and the tube bundle diameter is measured as 9/32-inch. In other words, when $\frac{d_w}{C} \leq 0.445$, the turbulence produced by the promoter is inadequate to mix the shell side flow.

(3) Entrance length is approximately inversely proportional to the mixing parameter ϕ.

VI DISCUSSION OF TEST RESULTS

Friction Factors

Experimentally determined pure friction factors for axial flow through the tube bundle are presented in Figure (27) and are compared with the friction factor curves for conventional use from References (2) and (3). As shown in the figure, line A-B is cited from Reference (2) for commercial pipes, i.e., clean pipes of steel and cast iron and can be expressed by the following equation,

$$\frac{1}{\sqrt{f}} = 3.2 \log_{10} \left[N_{Re} \sqrt{f} \right] + 1.2 \qquad (10)$$

Line C-D is for smooth pipes (glass, copper and most drawn tubing) and may be expressed as,

$$f = 0.0014 + \frac{0.125}{(N_{Re})^{0.32}} \qquad (11)$$

for the range of Reynolds numbers 3,000 to 3,000,000. Line E-F is taken from Moody's curves[3] and plotted from the equation of Colebrook and White [4], for the relative roughness, $\frac{\varepsilon}{D_e} = 0$

$$\frac{1}{\sqrt{f}} = 1.74 - 2 \log_{10} \left(\frac{2\varepsilon}{D_e} + \frac{18.7}{N_{Re}\sqrt{f}} \right) \qquad (12)$$

Where ε is defined as absolute roughness of the pipe inner surface. Line E-G and E-H are plotted from the above equation for $\frac{\varepsilon}{D_e} = 0.0001$ and $\frac{\varepsilon}{D_e} = 0.0004$ respectively.

Line I-J is calculated from the Blasius friction factor correlation expressed in Equation (8) for smooth pipes in the range of Reynolds number 3,000 to 100,000.

Finally line K-L is the result reduced from 60 data points of the present test.

As shown in the figure, it is seen that the experimental friction factors from the present test lie approximately 10 to 20% below all the conventional predictions for smooth pipes. The difference between tube-bundle and tube friction factors may be explained partially by errors in flow area, flow rate and equivalent diameter measurements, but these errors (estimated to be about 11% in Appendix B) are not large enough to explain the entire difference. It may be that the semi-empirical concept of hydraulic equivalent diameter for noncircular flow passage is not exactly correct for a flow cross section of the present test so different from a round tube. In other words, the fact that the pressure drop is exactly inversely proportional to D_e is no longer true in the case where the flow passage deviates too much from the round circular shape. It is thought that more geometrical quantities have to be considered in the pressure drop correlation for the tube-bundle case, and pitch to diameter ratio of the tube bundle seems to be the most likely nondimensional parameter to be considered.

The experimental friction factors for perturbed axial flow passing the tube bundle are presented in Figures (14) to (16). After an examination of this test data a correlation can be made over the Reynolds numbers range of 18,000 to 38,000 as follows,

$$f_{wc} = (1 + 1.25\phi)\, f_{ax} \qquad (13)$$

where ϕ is the previously defined turbulent mixing parameter.

Loss Coefficients

The experimental results for spacer loss coefficients as functions of Reynolds numbers are presented in Figures (20) to (23) and the results for exit loss coefficient in Figure (25). For the purpose of comparison, a new plot of loss coefficients which were evaluated based upon the shell side velocity head is presented in Figure (28). In this figure, the symbol I indicates the experimental scattering of the test data. Most of the loss coefficients showed a slight decrease with increasing Reynolds number as might be expected.

In Figure (29), an interesting plot of the spacer loss coefficient as a function of the net flow area is presented. This net flow area ratio is defined as follows:

$$\frac{(A_F)_{sp}}{(A_F)_{sh}} = \frac{\text{Net Flow Area Inside the Spacer}}{\text{Net Flow Area in Shell Side}}$$

As expected, the curve in Figure (29) shows a fairly sharp increase in the loss coefficient as the net flow area ratio is decreased.

Conventional methods in predicting loss coefficient for fluid flowing through passages subject to cross sectional or directional changes are generally accomplished by summarizing rather complex combinations of contraction loss, expansion loss, turning loss and so forth. For instance, the flow through a spacer must first undergo a contraction into a smaller flow area then followed immediately by an expansion to the larger shell side flow area. No attempt has been made to predict these loss coefficients for comparison with the present data since their complex nature would make agreement accidental.

Error Analysis

In Appendix (B), a complete error analysis is presented. The experimental error in evaluating friction factors and loss coefficients are summarized as follows:

Test Results	Maximum Possible Errors
f_{ax}	11%
f_{wc}	10%

Test Results	Maximum Possible Errors
(K_{sp}) Spacer #1	15%
(K_{sp}) Rod Spacer	8%
K_{eh}	8%
K_{em}	26%

VII CONCLUDING REMARKS

Experimental information on shell side hydraulic characteristics for a full-scale SNAP-8 Multiple Tube Model Boiler has resulted from this investigation. The pressure losses for the shell side flow passing through various passages have been measured and correlated. Both friction factors for the shell side flow passing the tube bundle with or without turbulence promoters and loss coefficients for different kinds of tube supporting spacers and exit manifolds have been experimentally determined. The general conclusions resulting from this investigations are drawn as follows:

1. Friction factors for shell side axial flow passing through the tube bundle are found to be about 10 - 20% lower than the values predicted by conventional empirical equations for smooth pipes. The pitch to diameter ratio seems to be the most appropriate nondimensional parameter to be added to the conventional pressure drop correlations.

2. Friction factors for shell side pertrubed axial flow passing through the tube bundle can be predicted by multiplying a coefficient group with the value for pure axial flow, i.e.,

$$f_{wc} = (1 + 1.25\phi)\, f_{ax}$$

over the Reynolds number range of 18,000 to 38,000. Where ϕ is defined as the turbulent mixing parameter in equation (9).

3. Both friction factors and loss coefficients are found to slightly decrease when increasing the Reynolds number.

(4) Pressure loss in the perturbed axial flow region was found to be directly proportional to the turbulence promoter size (copper wire coils wrapped around the tube bundle have been used as the turbulence promoters) and inversely proportional to the wrapping pitch.

(5) The mixing effect induced by the turbulence promoter is found to be directly proportional to the wire coil size and inversely proportional to the wire wrapping pitch.

(6) An increase in pressure loss for the spacers is found when the mixing level of the upstream incoming flow is increased. A typical example shows that if installing a turbulence promoter (1/4-inch x 3-inch copper wire coil) in the upstream, the pressure loss for the spacer is about 20% higher than that value when there is no turbulence promoter in the upstream.

(7) About 90% of the total exit loss was found to have occurred when the flow passes through the shell tube radial ports which were designed to meet the requirement of uniform shell side flow distribution in the exit region. In addition, the total exit pressure loss was also found to be a weak function of upstream mixing level induced by the turbulence promoters.

(8) Selection of the shell side turbulence promoter is a compromise between pressure loss and mixing effect. With reasonable pressure loss, the best choice manifested by the present test seems to be a 3/16-inch diameter wire coil with 6-inch pitch. A fully developed mixing of the shell side flow was visualized after two or three turns of the wrapping wire coil or 15 to 20 inches from the start of the wire coil.

APPENDIX (A) TABULATION OF TEST DATA

(1) Axial Flow Passing Tube Bundle $(\triangle P)_I$

W_{H_2O}	$N_{Re} \times 10^{-4}$	$(\triangle P)_I$ (Psi)									
lb/sec	← TESTING RUNS →										
9.1	1.84	0.038	0.038	0.0325	0.0298	0.0312	0.0339	0.027	0.032	0.027	0.029
12.3	2.48	0.054	0.057	0.0535	0.0551	0.0583	0.057	0.053	0.051	0.049	0.053
15	3.02	0.079	0.076	0.0786	0.0759	0.085	0.081	0.076	0.076	0.073	0.074
17	3.43	0.0975	0.0975	0.095	0.0975	0.106	0.10	0.095	0.10	0.095	0.095
19	3.83	0.122	0.121	0.133	0.119	0.121	0.119	0.103	0.119	0.114	0.119

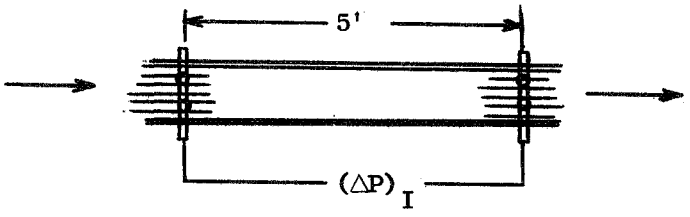

(2) Axial Flow Passing Spacers $(\triangle P)_{II}$

W_{H_2O}	$N_{Re} \times 10^{-4}$	$(\triangle P)_{II}$ (Psi)									
lb/sec	← SPACER #1 →						← ROD SPACER →				
9.1	1.84	0.033	0.035	0.035	0.038	0.034	0.04	0.104	0.106	0.088	0.089
12.3	2.48	0.057	0.067	0.072	0.067	0.065	0.075	0.162	0.171	0.157	0.157
15	3.02	0.086	0.095	0.097	0.098	0.092	0.106	0.244	0.242	0.222	0.22
17	3.43	0.11	0.12	0.14	0.13	0.12	0.13	0.315	0.325	0.296	0.294
19	3.83	0.146	0.144	0.17	0.154	0.146	0.161	0.415	0.41	0.366	0.378

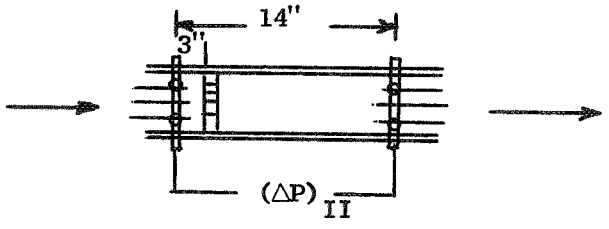

(3) Perturbed Axial Flow Passing Through Bundle, $(\Delta P)_{III}$

W_{H_2O}	$N_{Re} \times 10^{-4}$	$(\Delta P)_{III}$ (Psi)								
		← Wire Coil Combinations →								
lb/sec		(1/4x3)	(1/4x6)	(1/4x10)	(1/4x20)	(3/16x3)	(3/16x6)	(3/10x10)	(3/10x20)	(1/8x3)
9.1	1.84	0.184	0.109	0.087	0.076	0.15	0.079	0.064	0.042	0.073
12.3	2.48	0.298	0.205	0.155	0.098	0.246	0.14	0.113	0.087	0.096
15	3.02	0.445	0.323	0.207	0.142	0.344	0.209	0.161	0.121	0.138
17	3.43	0.577	0.425	0.285	0.183	0.464	0.276	0.204	0.153	0.174
19	3.83	0.74	0.531	0.352	0.241	0.581	0.36	0.257	0.19	0.225

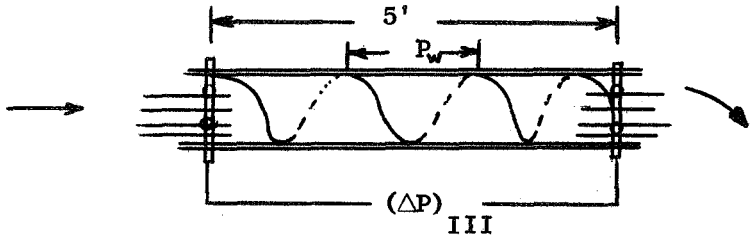

(4) Perturbed Flow Passing Spacers, $(\Delta P)_{IV}$

W_{H_2O}	$N_{Re} \times .0^{-4}$	$(\Delta P)_{IV}$ (Psi)								
		← Upstream Flow Mixing Parameter ϕ →								
lb/sec		3.92	2.08	1.41	0.985	2.22	1.18	0.96	0.795	.058
		← ROD SPACER →				← SPACER #1 →				
9.1	1.84	0.113	0.103	0.097	0.089	0.039	0.034	0.033	0.031	0.029
12.3	2.48	0.214	0.208	0.174	0.193	0.065	0.06	0.056	0.05	0.042
15	3.02	0.296	0.271	0.253	0.241	0.089	0.084	0.083	0.079	0.066
17	3.43	0.389	0.36	0.354	0.315	0.116	0.106	0.101	0.091	0.09
19	3.83	0.465	0.448	0.41	0.38	0.148	0.131	0.128	0.12	0.126

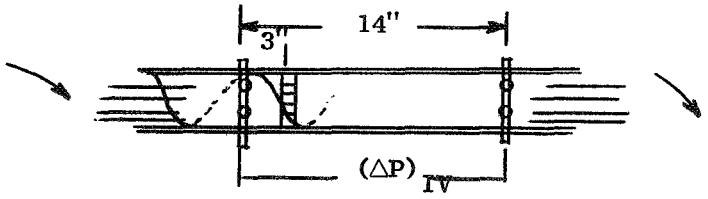

(5) Shell Side Flow Passing Through the Exit Radial Ports, $(\Delta P)_V$

W_{H_2O}	$N_{Re} \times 10^{-4}$	$(\Delta P)_V$ (Psi)								
		← Upstream Flow Mixing Parameter, ϕ →								
lb/sec		3.92	2.22	2.08	1.41	1.18	0.985	0.96	0.795	0.58
9.1	1.84	0.0765	0.089	0.078	0.084	0.083	0.078	0.086	0.06	0.07
12.3	2.48	0.168	0.165	0.168	0.160	0.17	0.161	0.154	0.171	0.161
15	3.02	0.246	0.241	0.25	0.238	0.246	0.233	0.228	0.263	0.236
17	3.43	0.329	0.319	0.346	0.318	0.336	0.318	0.314	0.344	0.304
19	3.83	0.431	0.486	0.438	0.404	0.453	0.421	0.378	0.428	0.382

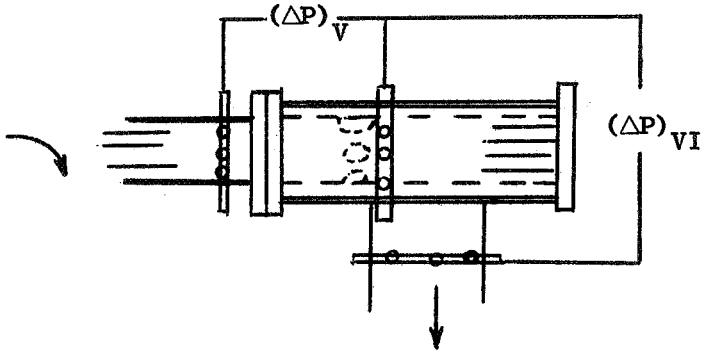

(6) Shell Side Flow Passing the Exit Manifold $(\Delta P)_{V1}$

W_{H_2O}	$N_{Re} \times 10^{-4}$	$(\Delta P)_{V1}$ (Psi)								
		← Upstream Flow Mixing Parameter, ϕ →								
lb/sec		3.92	2.23	2.08	1.41	1.18	0.985	0.96	0.795	0.58
9.1	1.84	0.0081	0.0063	0.089	0.007	0.0066	0.0085	0.0061	0.0054	0.0041
12.3	2.48	0.0185	0.0171	0.019	0.018	0.0162	0.018	0.0176	0.0125	0.015
15	3.02	0.0312	0.028	0.035	0.0298	0.0203	0.0298	0.0305	0.028	0.036
17	3.43	0.0434	0.041	0.051	0.049	0.0398	0.0352	0.038	0.038	0.043
19	3.83	0.0543	0.053	0.065	0.063	0.048	0.0515	0.0595	0.054	0.056

(7) Pressure Loss Across Spacer #1* (Upstream Axial Flow Only)

W_{H_2O} (lb/sec)	10	10.5	11	11.8	12	12.2	12.8	13.4	13.8	14.5	15	16
ΔP(Psi)	.07	.076	.08	.096	.099	.102	.115	.12	.135	.155	.157	.175

(8) Pressure Loss Across the Exit Manifold Assembly*

W_{H_2O} (lb/sec)	10	10.5	11.8	12.2	12.8	13.8	14.5	16.1
ΔP(Psi)	0.178	0.214	0.251	0.268	0.301	0.371	0.43	0.485

* Data taken from the preliminary checkout test which was described in Contract NAS 3-10610, Monthly Status Report of March 10, 1969.

APPENDIX (B) ERROR ANALYSIS OF THE TEST DATA

The maximum error limit on the measured friction factors and loss coefficients have been estimated as follows:

The friction factor is calculated from the equation

$$f = \frac{\Delta P}{\left(\frac{L}{D_e}\right)\frac{1}{2g\rho}\left(\frac{W_{H_2O}}{A_F}\right)^2} \qquad \text{(A-1)}$$

Then the maximum error is given approximately by

$$\frac{df}{f} = \left\{\left[\frac{d(\Delta P)}{\Delta P}\right]^2 + \left[\frac{d(D_e)}{D_e}\right]^2 + \left[\frac{2d(A_F)}{A_F}\right]^2 + \left[\frac{d(L)}{L}\right]^2 + \left[\frac{2d(W_{H_2O})}{W_{H_2O}}\right]^2\right\}^{\frac{1}{2}} \qquad \text{(A-2)}$$

The following uncertainties are constant and estimated as;

Equivalent Diameter, $\frac{d(D_e)}{D_e} = 0.03$ or 3%

Shell Side Net Flow Are, $\frac{d(A_F)}{A_F} = 0.04$ or 4%.

Test Section Length, $\frac{d(L)}{L} = 0$ or zero percent error in L is assumed.

The percentage of errors made in the water flow rate is generally a function of the discharge coefficient of the orifice, the upstream pressure level of the orifice and the accuracy of the mercury manometer. For the present test, the maximum uncertainty in the measurement of water flow rate lies in the mercury manometer which has an accuracy known

to 0.05 inches of mercury. Then, the maximum error can be made for the water flow rate estimated at 5% for the lowest flow rates used in the test and 1% for the highest flow rates.

The error in the pressure measurement $\frac{d(\Delta P)}{(\Delta P)}$ is a function of the test section pressure drop. An error curve was presented in Figure (30) based upon an accuracy in the Meriam manometer reading known to 0.1 inches of Meriam fluid. Based upon this curve, the maximum errors occurring for each test section are listed as follows:

$$\frac{d(\Delta P_{ax})}{(\Delta P)_{ax}} = 0.07 \text{ or } 7\%$$

$$\left[\frac{d(\Delta P)}{\Delta P}\right]_{\text{spacer \#1}} = 0.13 \text{ or } 13\%$$

$$\left[\frac{d(\Delta P)}{\Delta P}\right]_{\text{rod spacer}} = 0.03 \text{ or } 3\%$$

$$\frac{d(\Delta P_{wc})}{\Delta P_{wc}} = 0.05 \text{ or } 5\%$$

$$\left[\frac{d(\Delta P)}{\Delta P}\right]_{\text{exit radial port}} = 0.03 \text{ or } 3\%$$

$$\left[\frac{d(\Delta P)}{\Delta P}\right]_{\text{exit manifold}} = 0.25 \text{ or } 25\%$$

Then, the friction factors for the present test are estimated to bear the following maximum errors

$$\frac{d(f_{ax})}{f_{ax}} = \left[(0.07)^2 + (0.03)^2 + (0.08)^2 + (0.02)^2\right] = 0.108 \text{ or } 10.8\%$$

$$\frac{d(f_{wc})}{f_{wc}} = 0.097 \text{ or } 9.7\%$$

and the loss coefficient is calculated from the equation

$$K = \frac{\Delta P}{\frac{1}{2g\rho}\left(\frac{W_{H_2O}}{A_F}\right)^2} \qquad \text{(A-3)}$$

the error in K can be written as

$$\frac{d(K)}{K} = \left\{ \left[\frac{d(\Delta P)}{\Delta P}\right]^2 + \left[\frac{d(2A_F)}{A_F}\right]^2 + \left[\frac{d(2W_{H_2O})}{W_{H_2O}}\right]^2 \right\}^{\frac{1}{2}} \qquad \text{(A-4)}$$

If the shell side net flow area A_F is used which has an estimated maximum error of 4% then we obtain

$$\left[\frac{d(K)}{K}\right]_{\text{spacer \# 1}} = 0.151 \text{ or } 15.1\%$$

$$\left[\frac{d(K)}{K}\right]_{\text{rod spacer}} = 0.083 \text{ or } 8.3\%$$

$$\left[\frac{d(K)}{K}\right]_{\text{exit radial ports}} = 0.083 \text{ or } 8.3\%$$

$$\left[\frac{d(K)}{K}\right]_{\text{exit manifold}} = 0.261 \text{ or } 26.1\%$$

It should be noted that the above estimate is based upon the shell side net flow area, A_F, which has an estimated error of 4%. When the net flow area passsing through spacer or exit manifold is used, one would expect that the error for K would be greater than the values shown above due to the increased difficulty in estimating flow area for a more complicated geometry.

REFERENCES

1. Converse, G. L. and Hsia, E.S. "Thermal and Hydraulic Anaylsis for Advanced SNAP-8 Boilers", HTC - 11, Nuclear Systems Programs - Missile and Space Division, General Electric Company, January, 1969.

2. McAdams, W.H. Heat Transmission McGraw-Hill Book Co., New York, Third Edition, 1954.

3. Moody, L.F. Friction Factors for Pipe Flow, ASME Trans. Vol.66, 1944, PP 671-684.

4. Eshback, O.(Editor), Handbook of Engineering Fundamentals, John Wiley and Sons, Inc., New York, Second Edition, 1952.

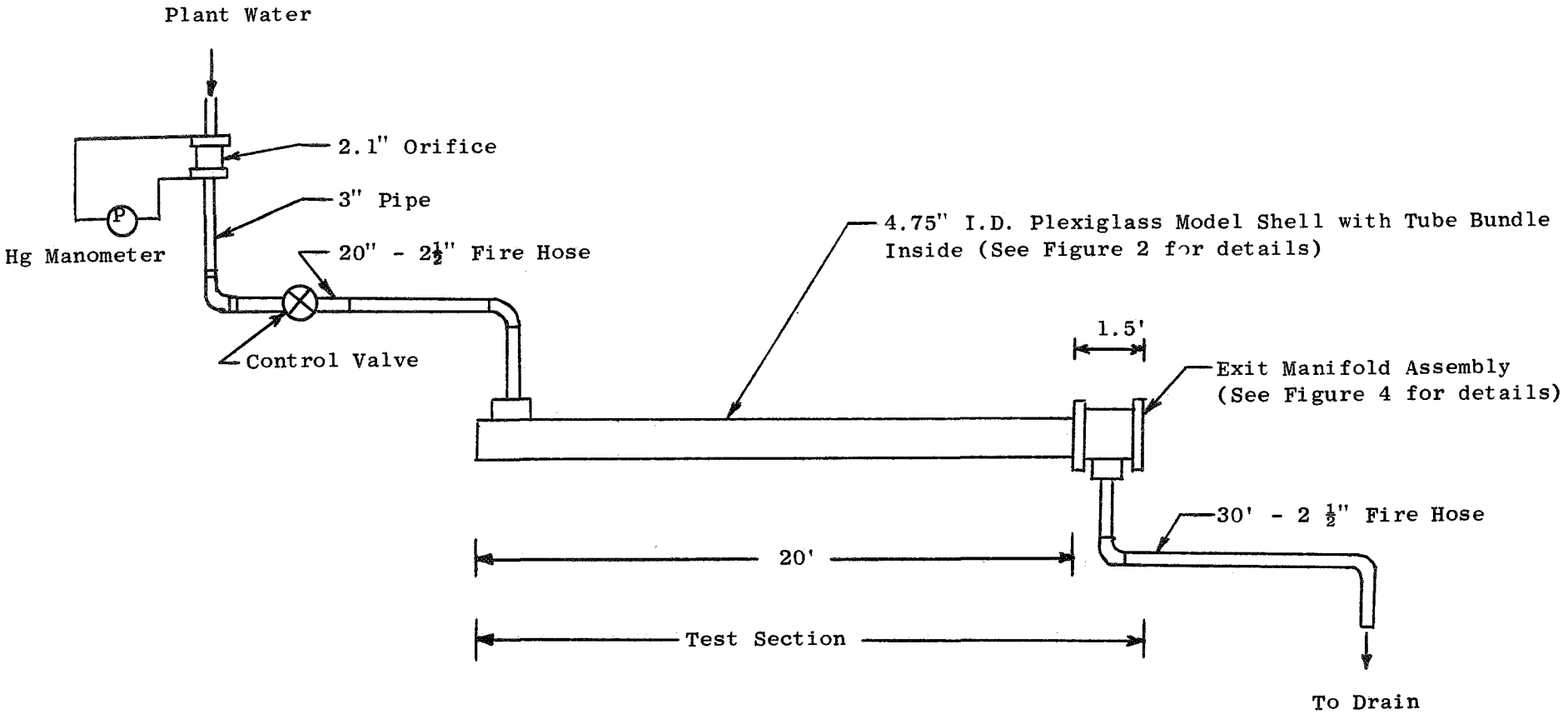

Figure 1. Schematic Diagram of Shell-side Hydraulic Test Setup.

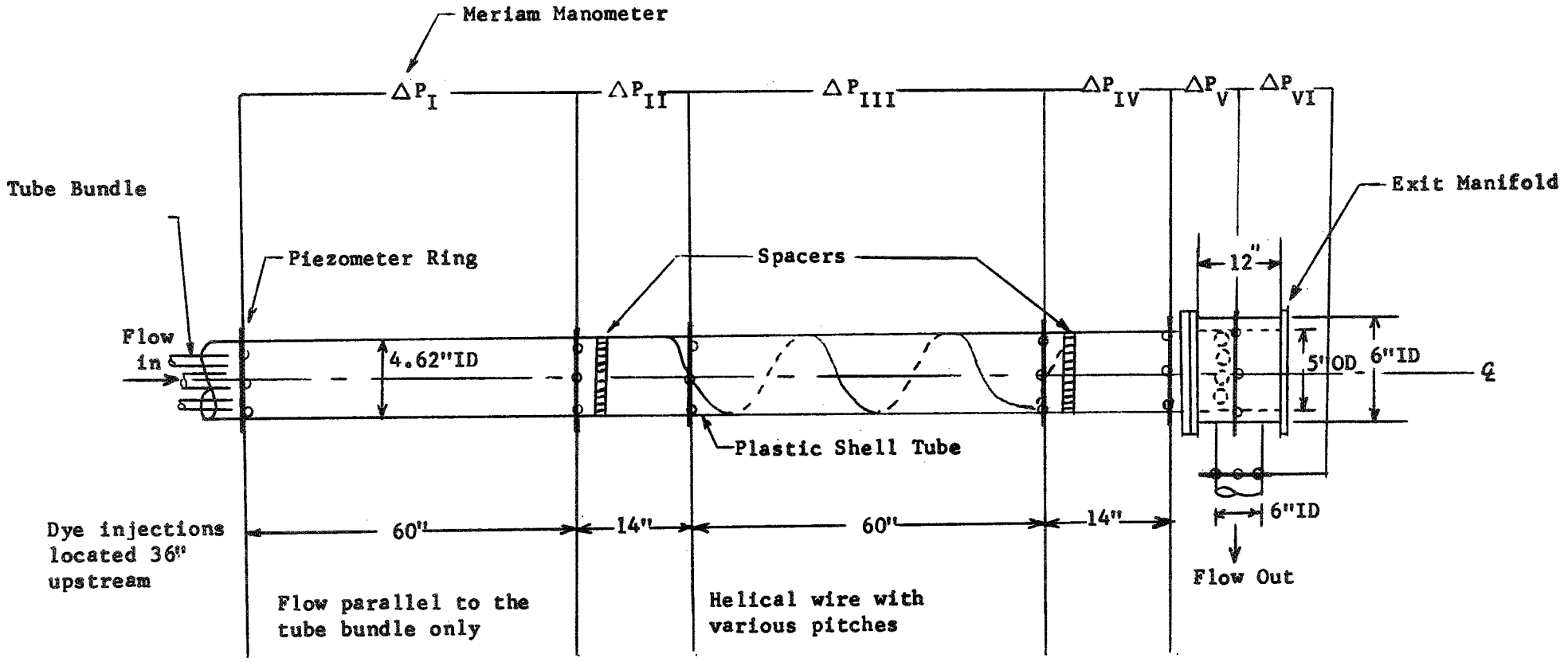

Figure 2 . Schematic Diagram of Model Boiler Shell-side Pressure Drop Measurement

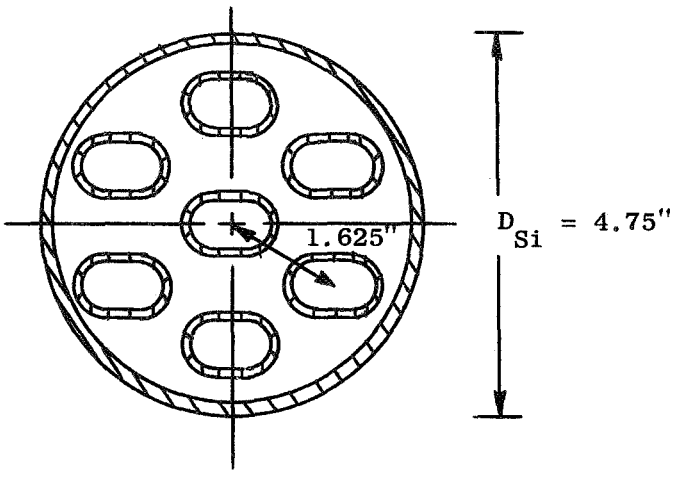

Model Boiler Cross Section with Plexiglass Shell

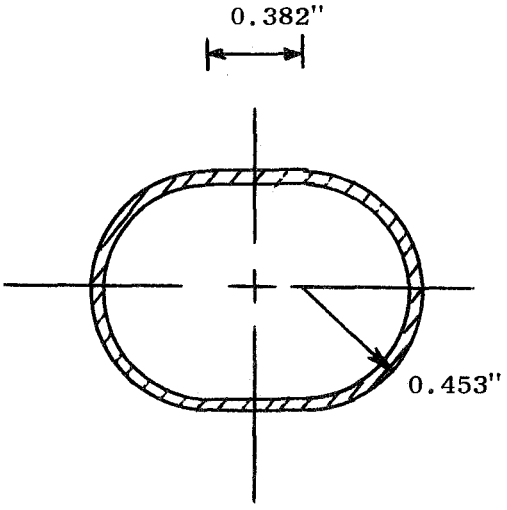

Stainless Steel Oval-Shaped Tube Cross Section

Figure 3. Model Boiler and Oval-Shaped Tube Cross Sections.

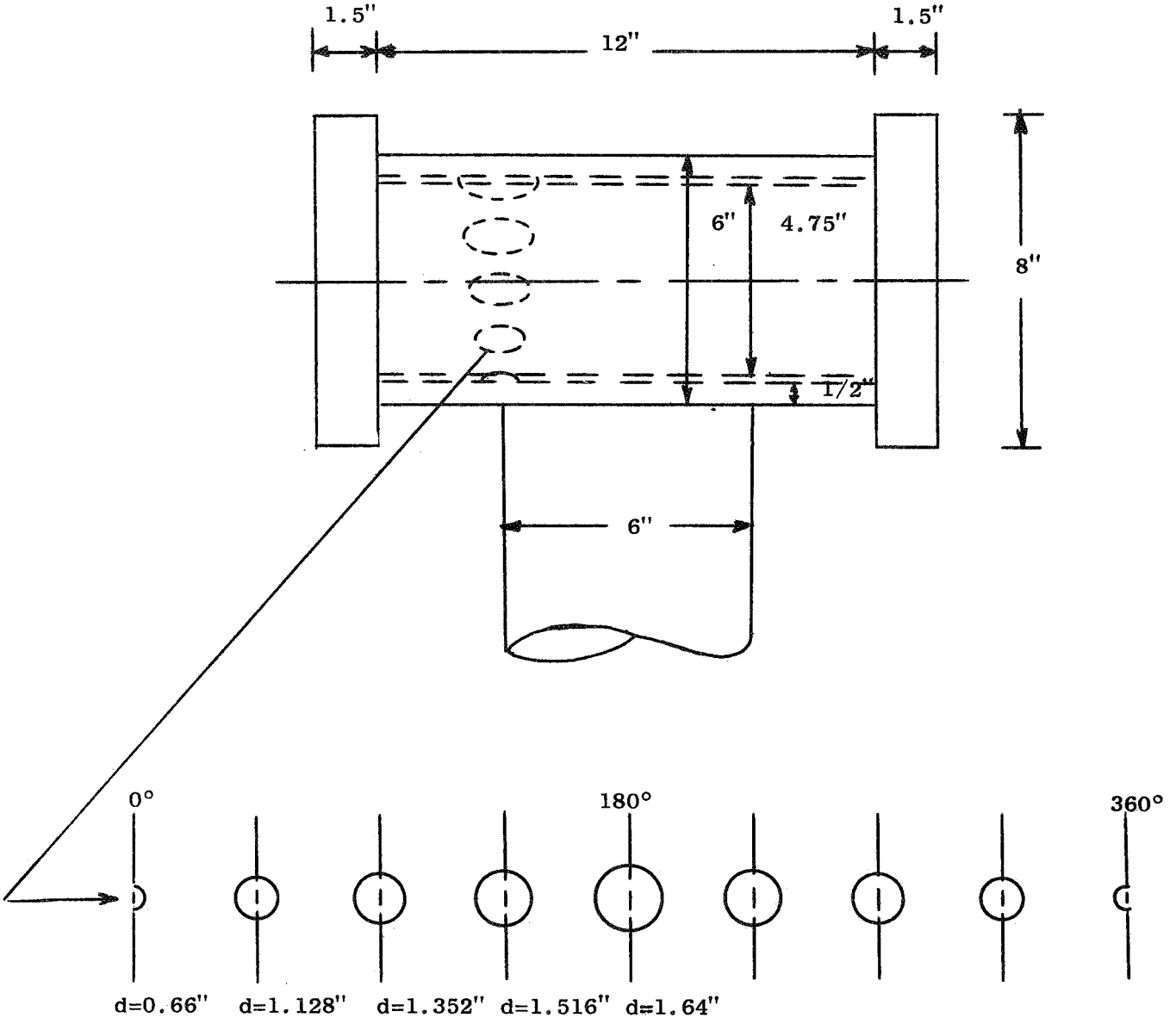

Note: 0° position facing the horizontal axial plane of the exit pipe.

Figure 4. Detailed Schematic of the Exit Manifold Assembly.

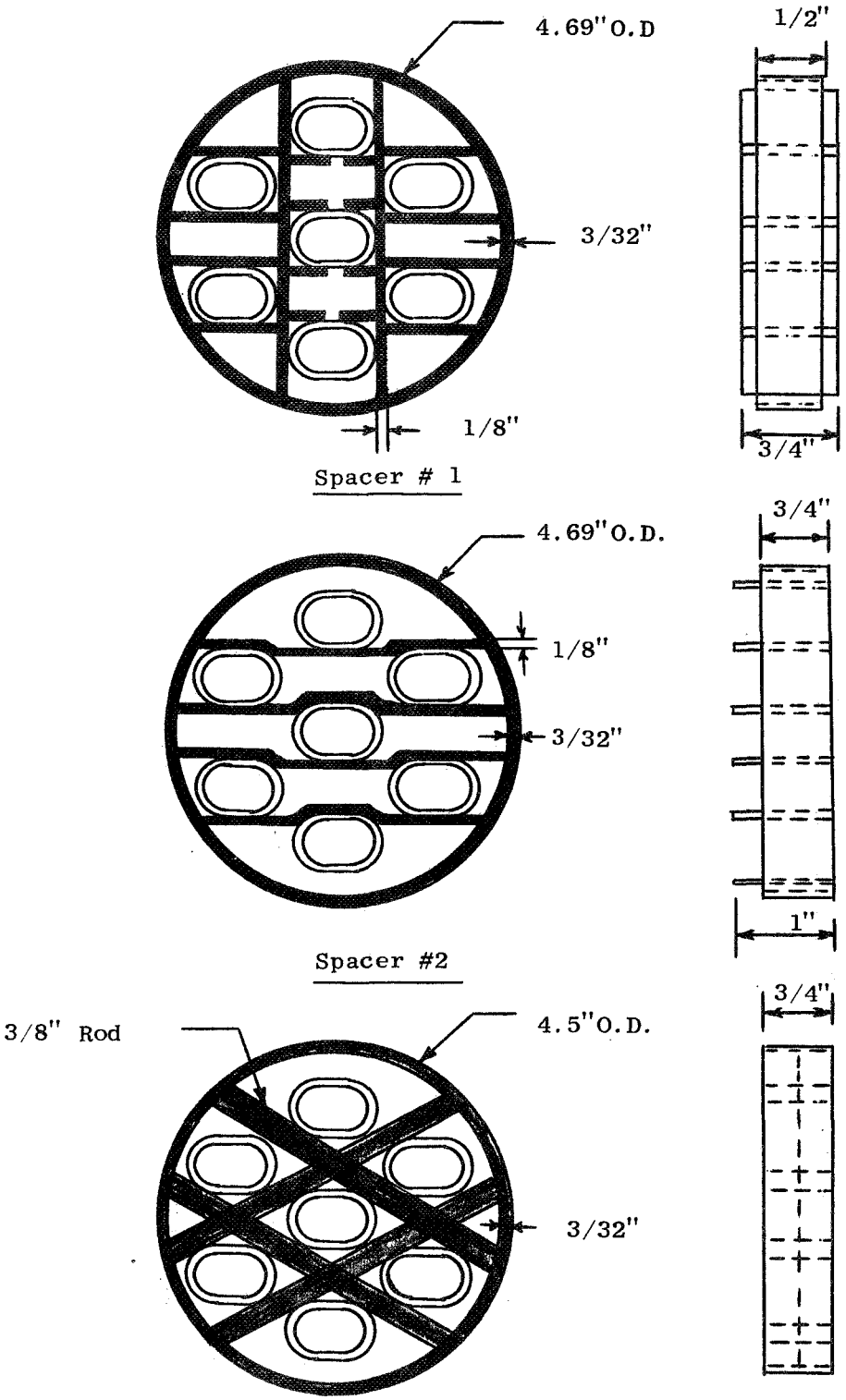

Figure 5. Schematic of Tube Bundle Supporting Spacers with Different Geometries (Note: All Spacers Material SS-314).

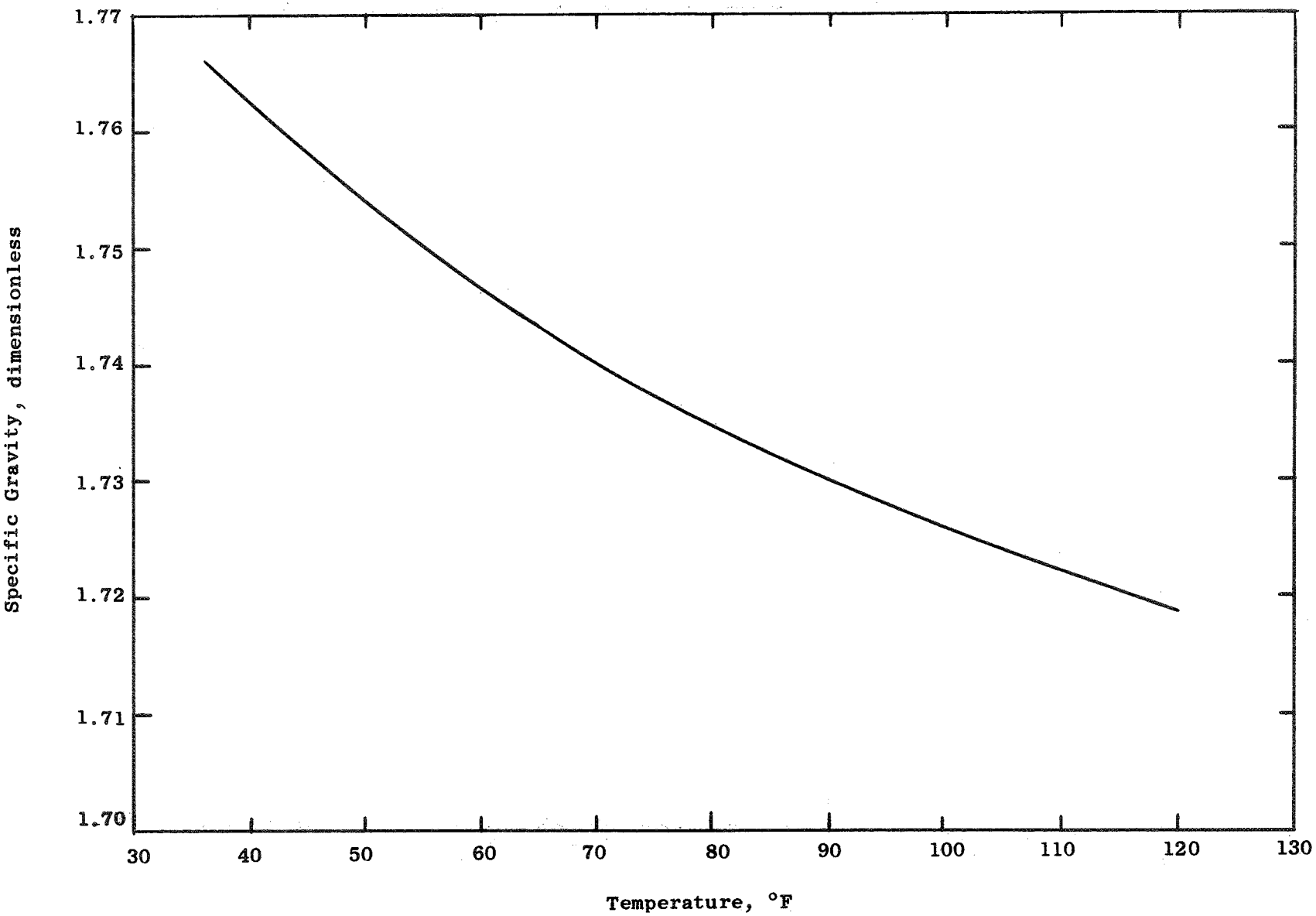

Figure 6. Specific Gravity vs. Temperature for Meriam D-8325 Indicating Fluid.

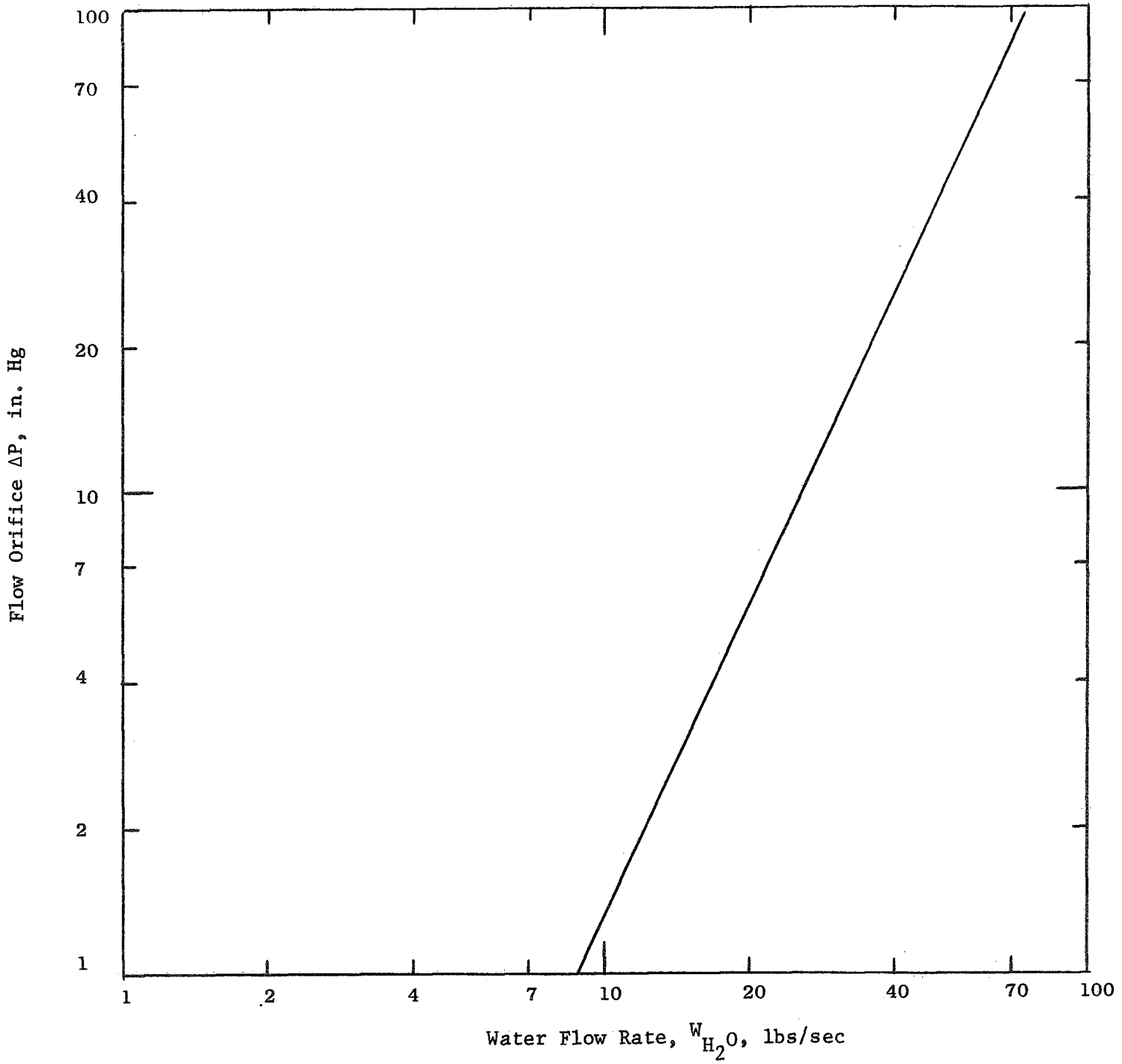

Figure 7. 2.1-inch Orifice Water Flow Calibration Curve.

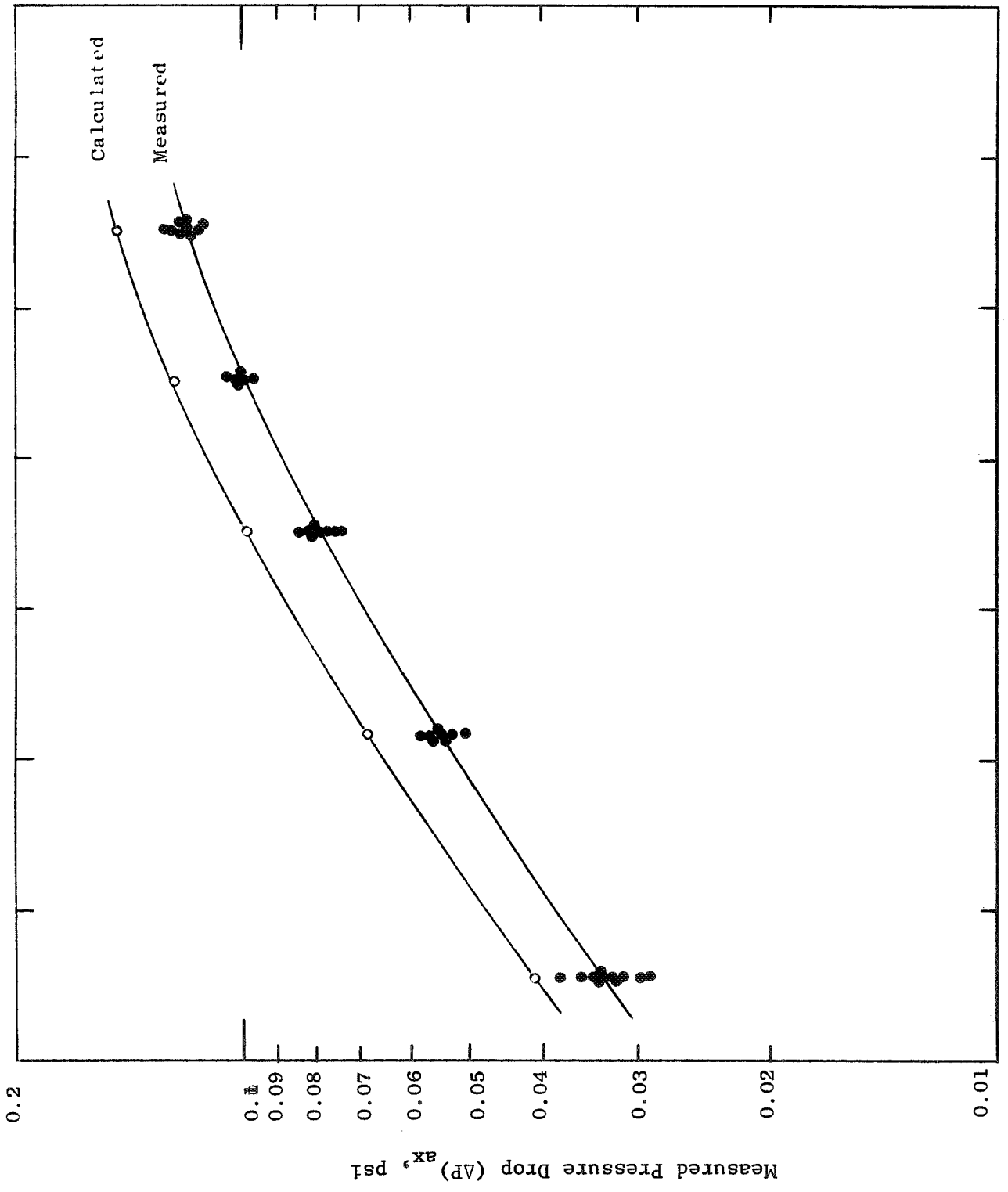

Figure 8. Measured Pressure Drop for Axial Flow Passing Tube Bundle over 5-Foot Tube Length.

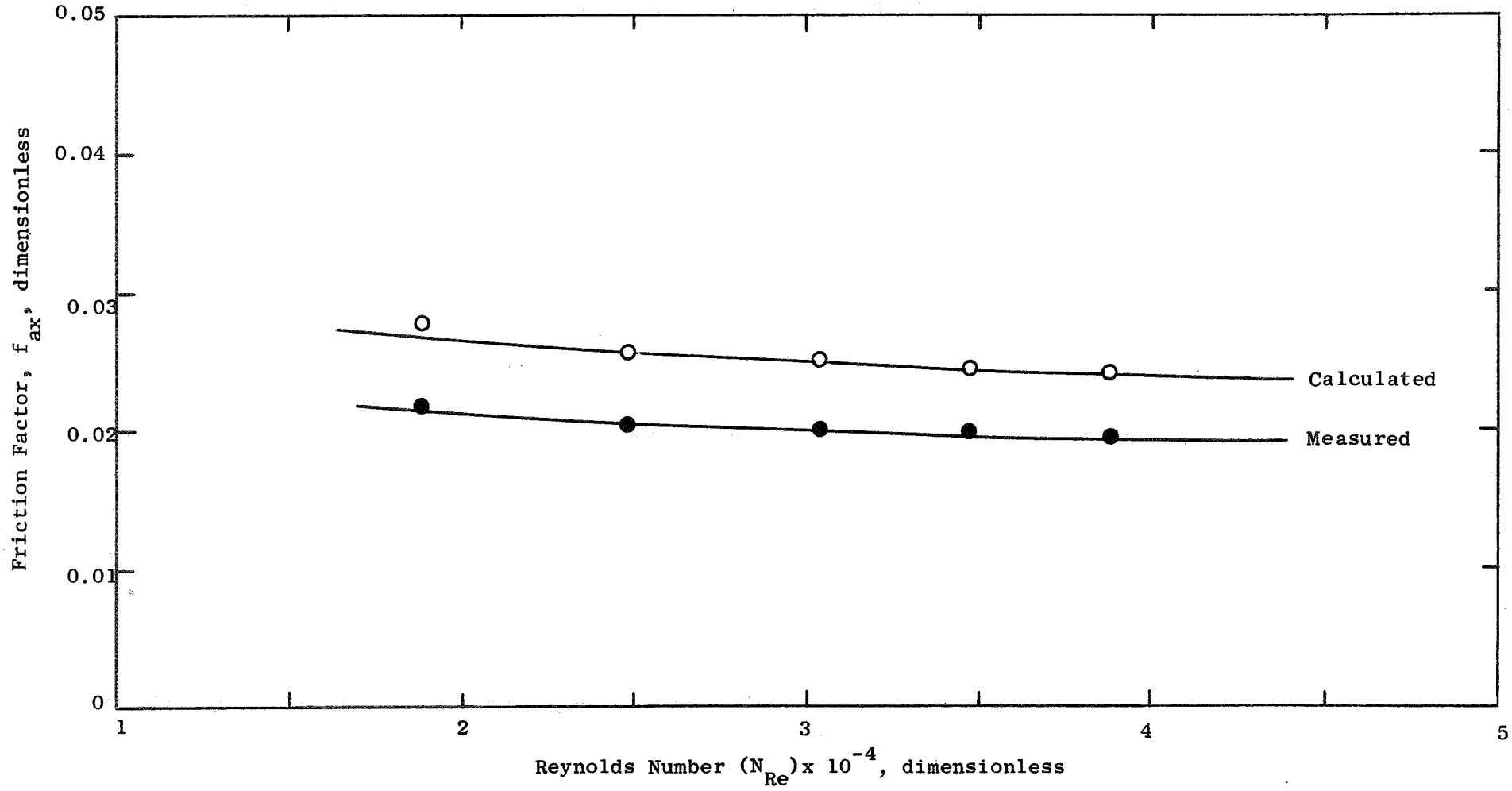

Figure 9. Measured Friction Factor for Axial Flow Passing Tube Bundle.

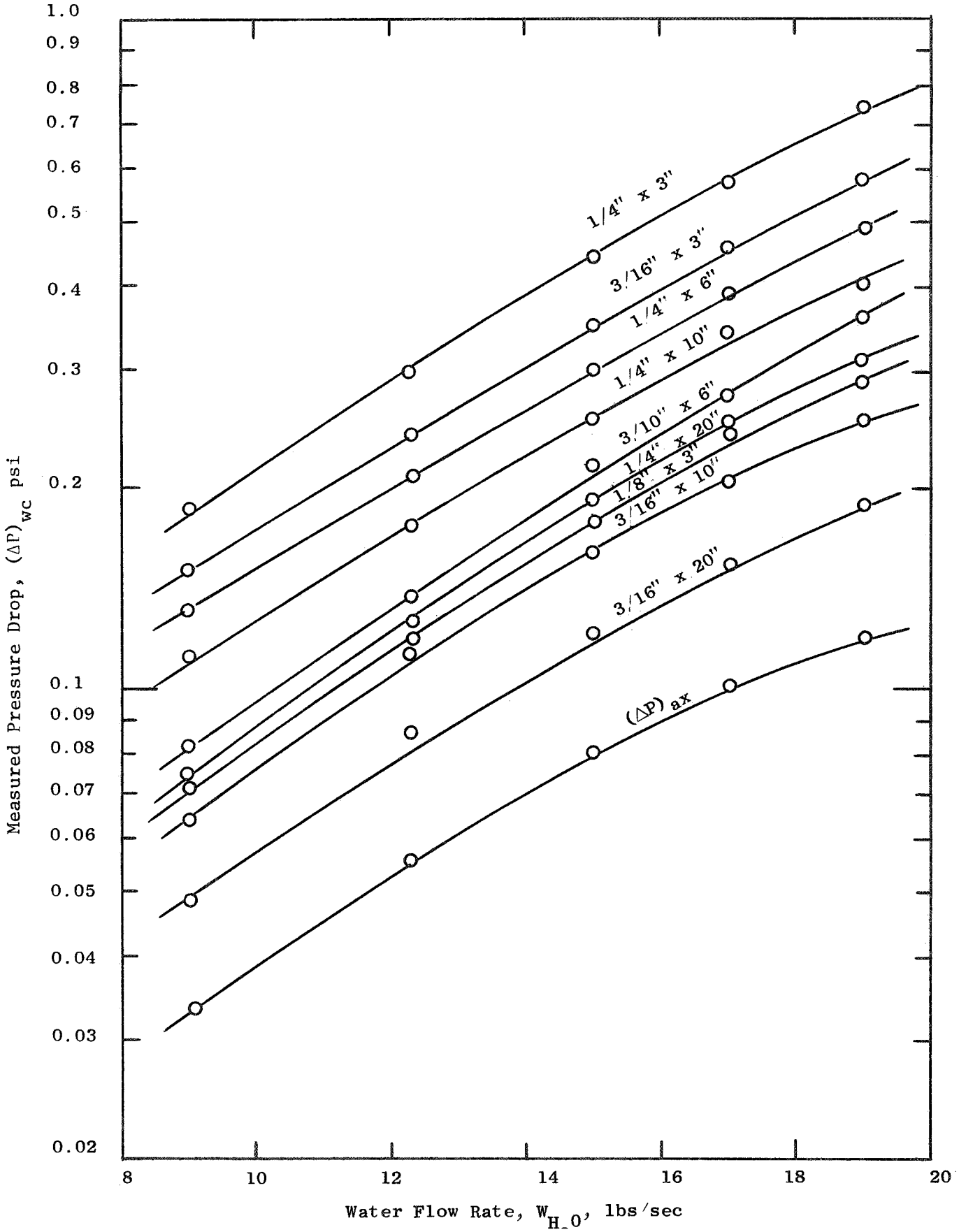

Figure 10. Measured Pressure Drop for Perturbed Axial Flow Passing Tube Bundle Over a 5-foot Tube Length for Various Turbulence Promoter Combinations.

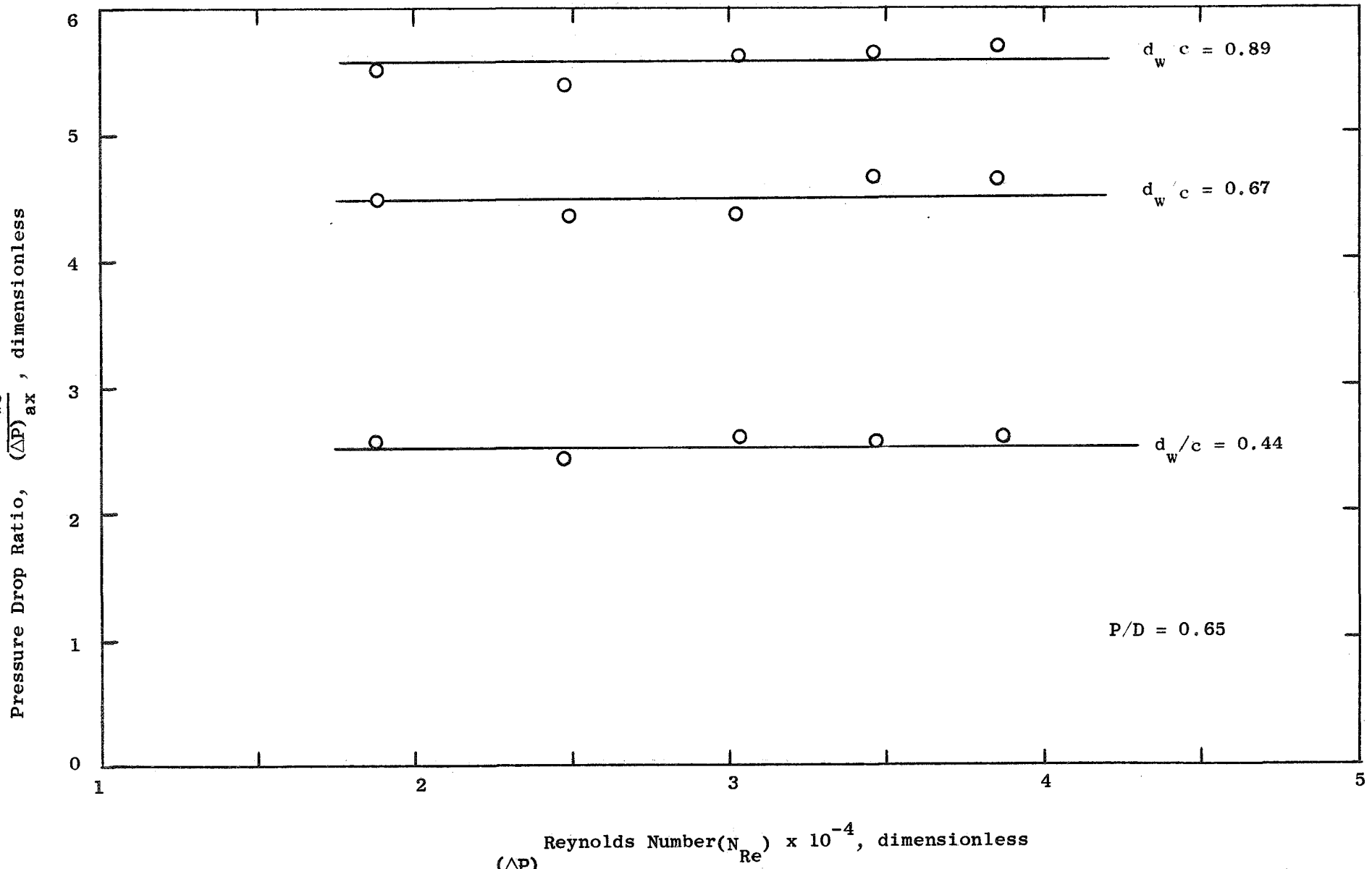

Figure 11. Pressure Drop Ratio, $\frac{(\Delta P)_{wc}}{(\Delta P)_{ax}}$ vs. Reynolds Number for Turbulence Promoters with P/D = 0.65

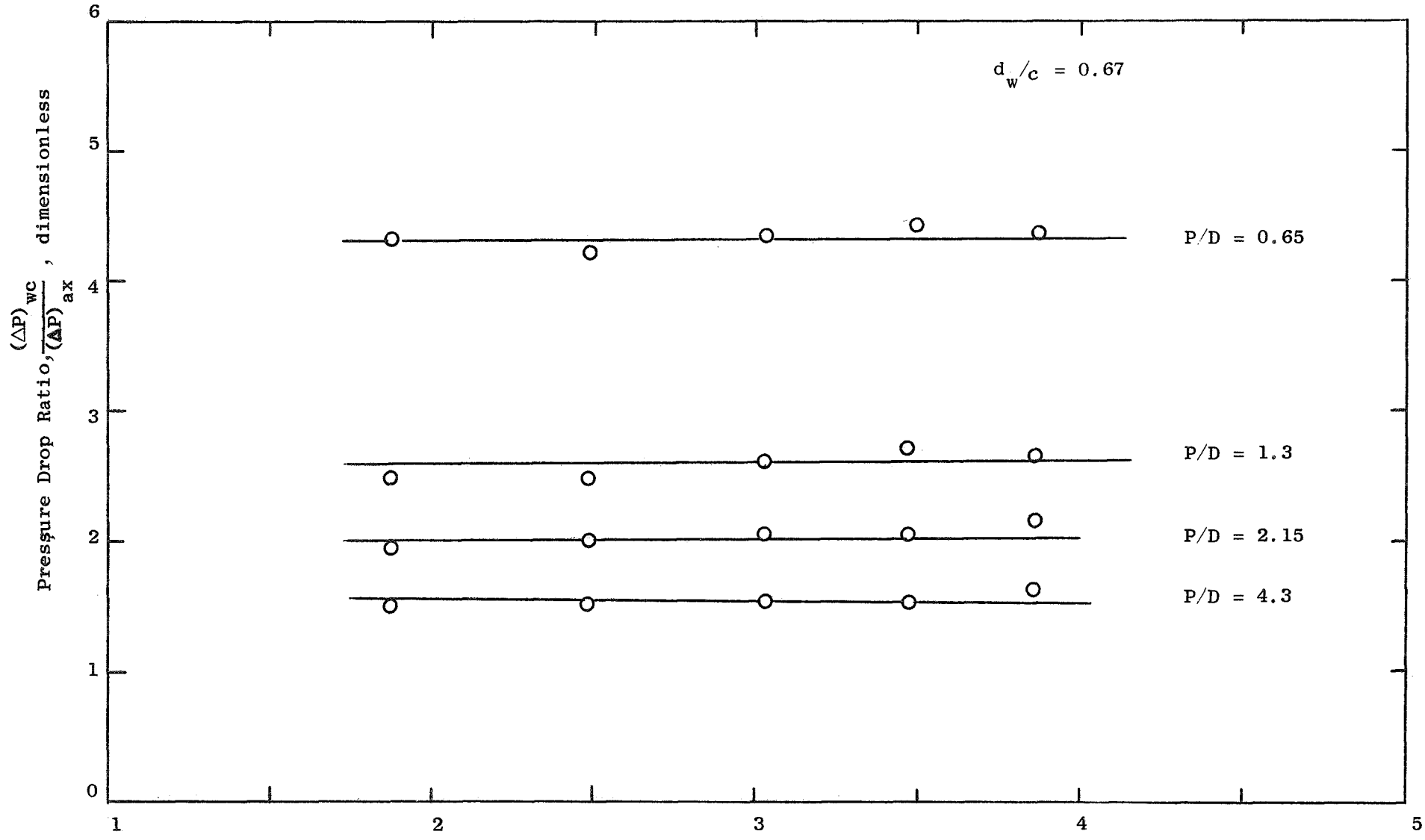

Figure 12. Pressure Drop Ratio, $\frac{(\Delta P)_{wc}}{(\Delta P)_{ax}}$ vs. Reynolds Number for Turbulence Promoters with $\frac{d_{wc}}{c} = 0.67$

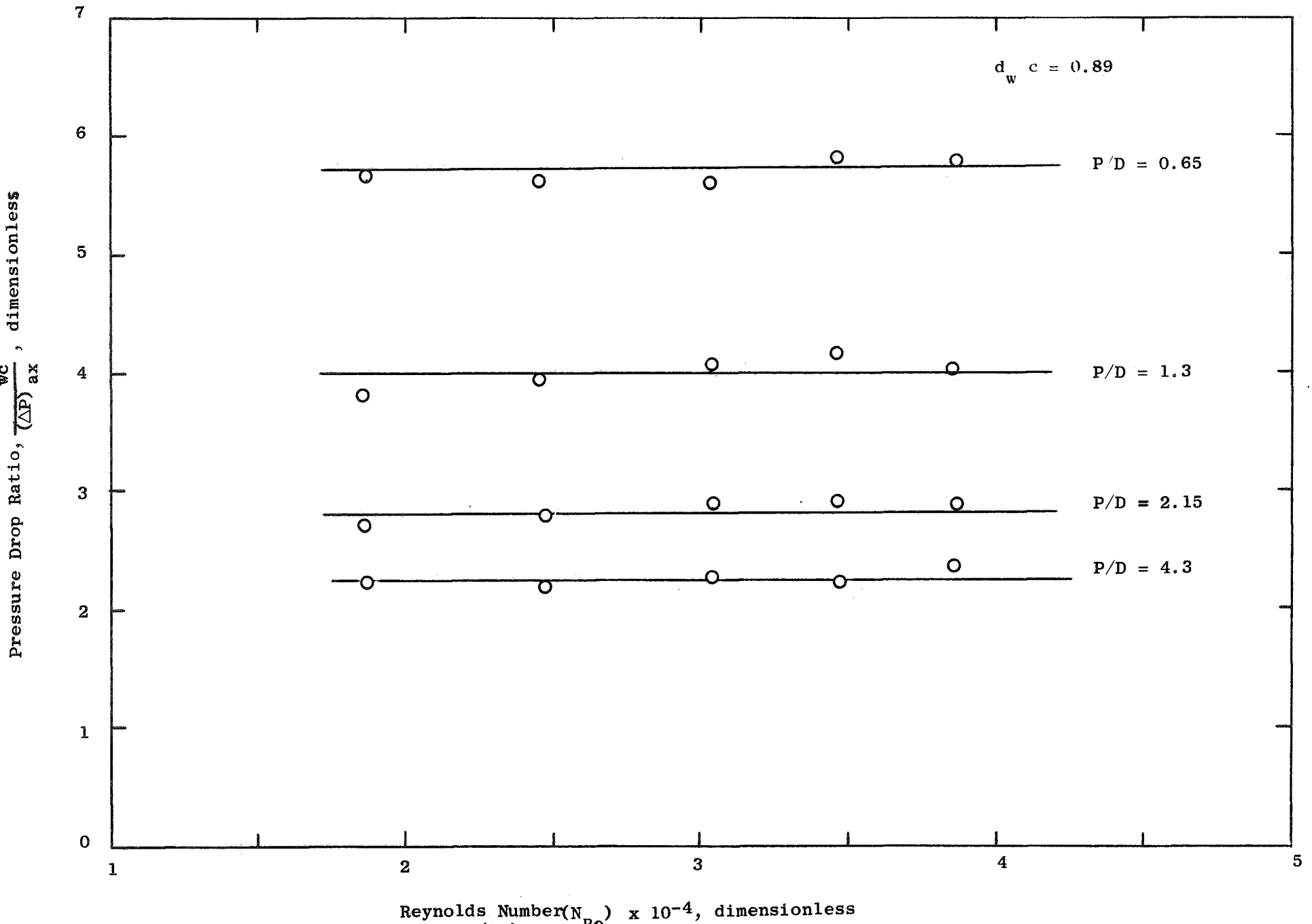

Figure 13. Pressure Drop Ratio, $\frac{(\Delta P)_{wc}}{(\Delta P)_{ax}}$ vs. Reynolds Number for Turbulence Promoters with $d_{wc}/c = 0.89$

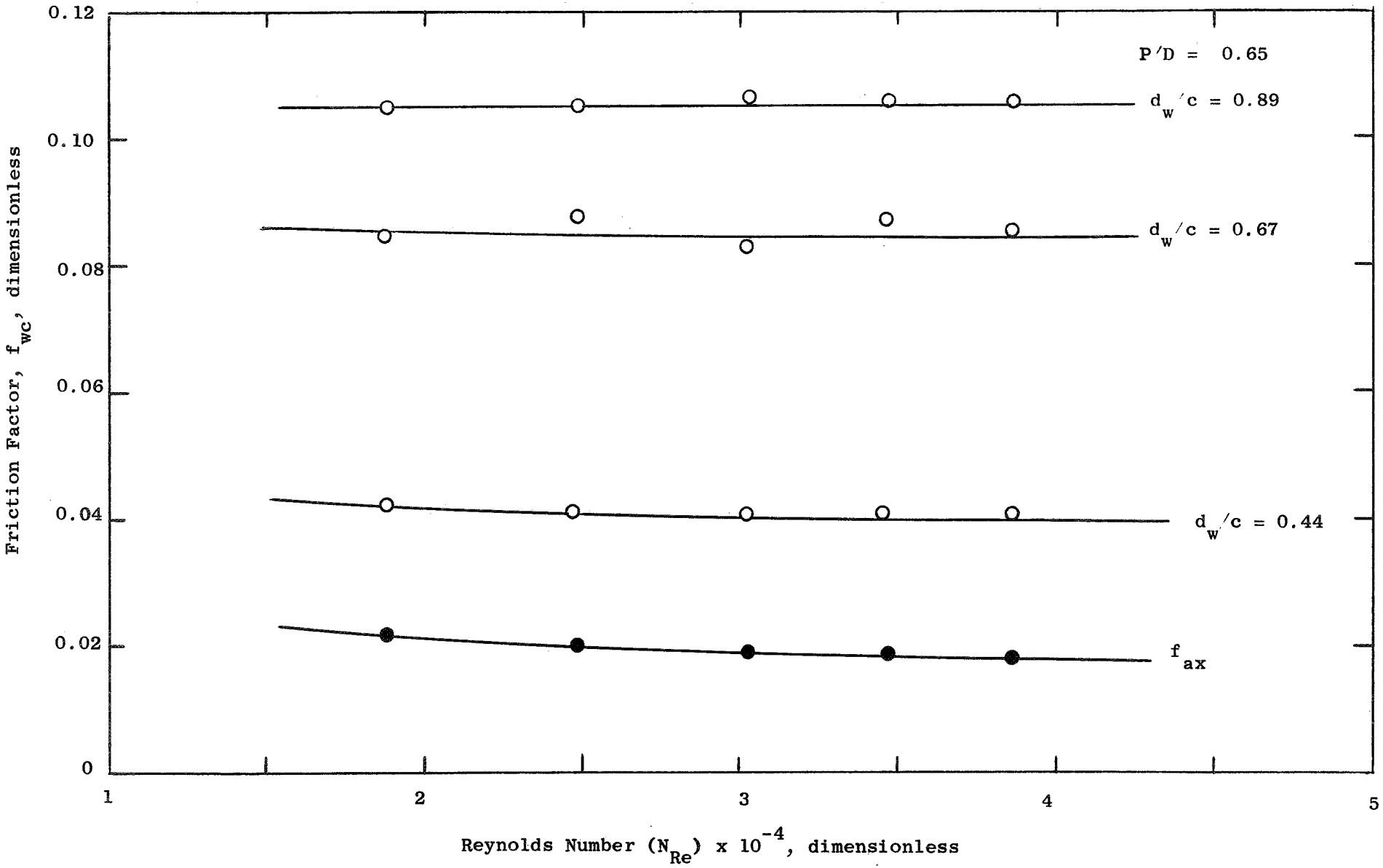

Figure 14. Measured Friction Factor for Perturbed Axial Flow Passing Tube Bundle for Turbulence Promoter with P/D = 0.65.

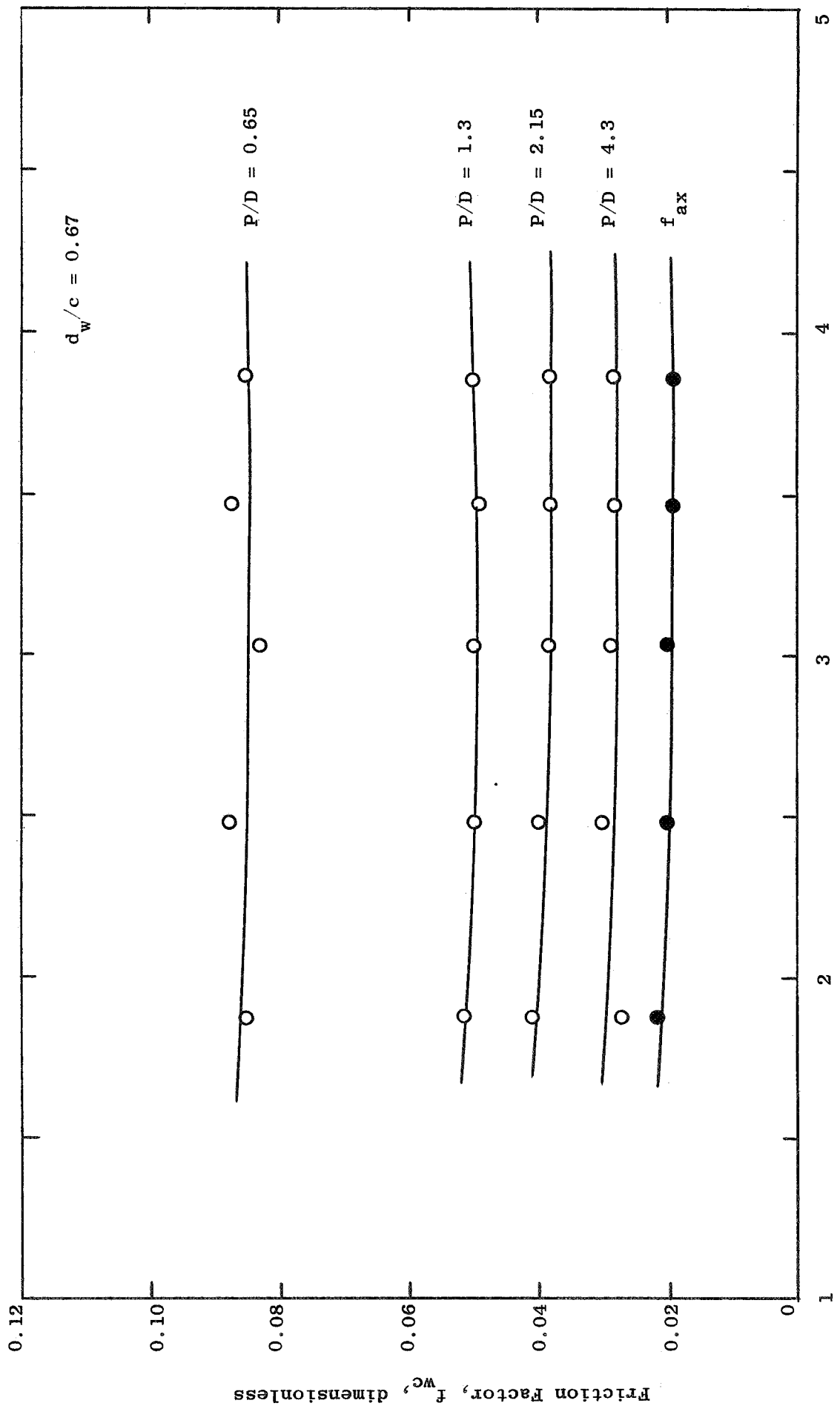

Figure 15. Measured Friction Factor for Perturbed Axial Flow Passing Tube Bundle for Turbulence Promoters with $d_w/c = 0.67$.

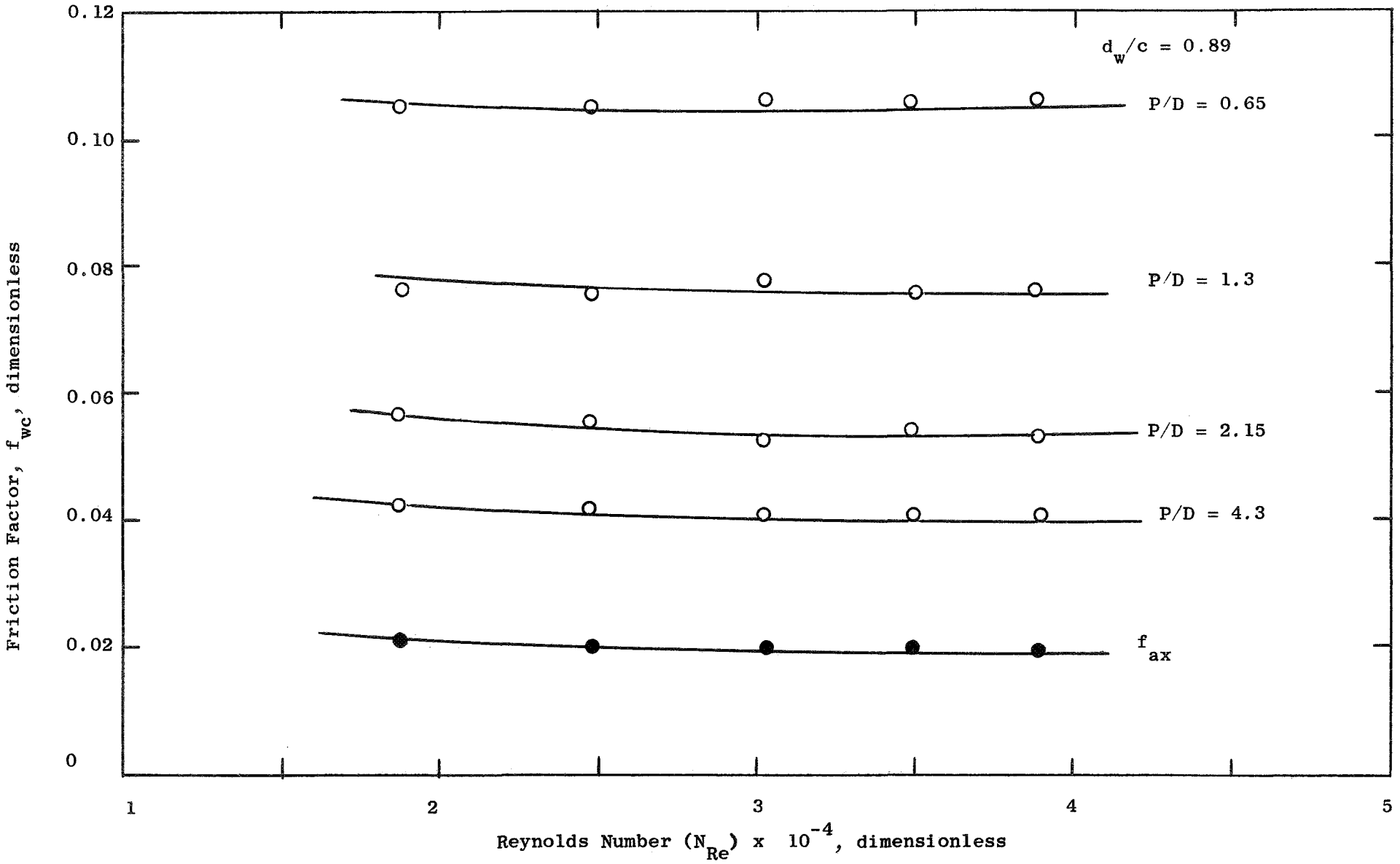

Figure 16. Measured Friction Factor for Perturbed Axial Flow Passing Tube Bundle for Turbulence Promoters with $d_w/c = 0.89$.

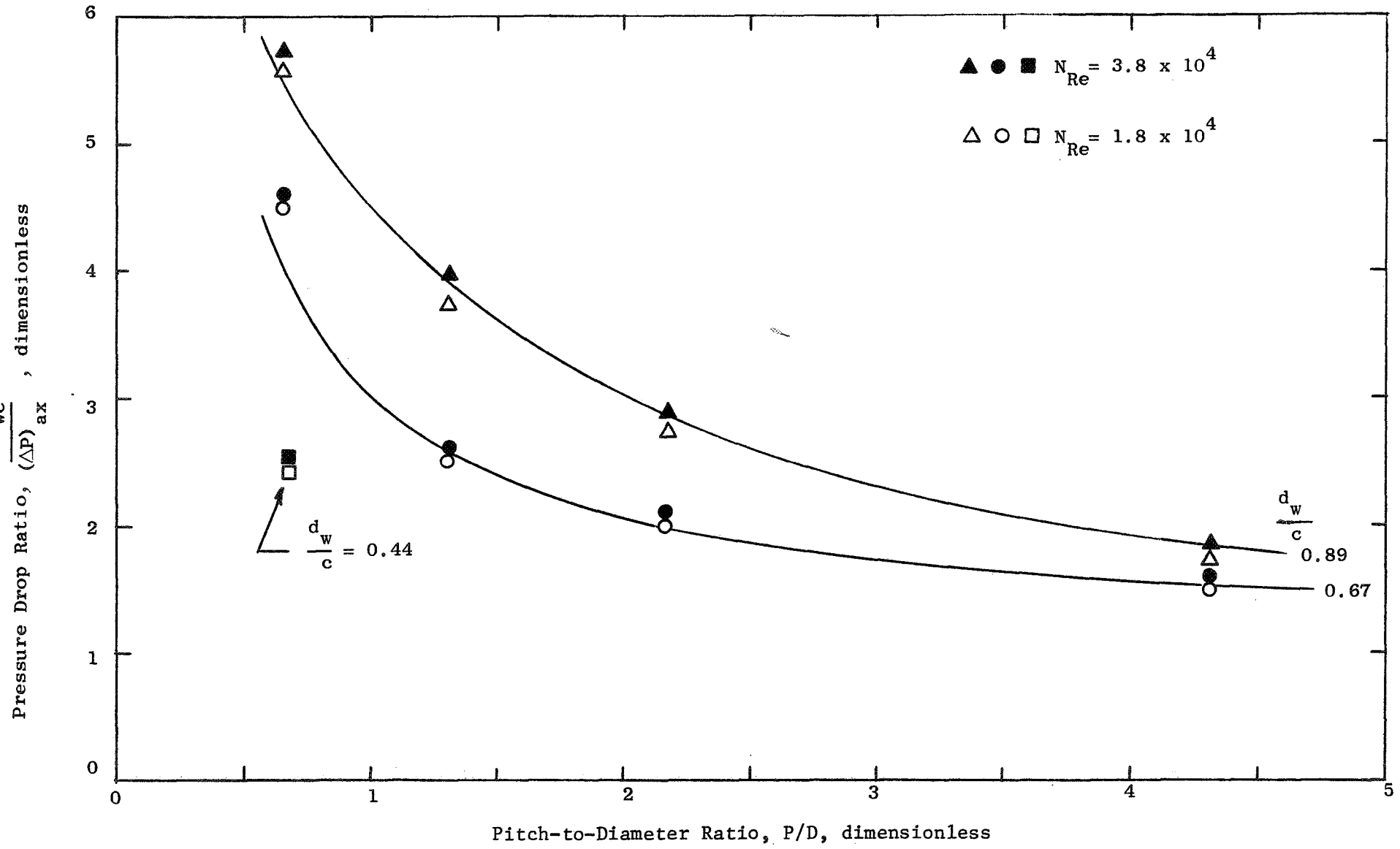

Figure 17. Pressure Drop Ratio $(\Delta P)_{wc}/(\Delta P)_{ax}$ vs. Turbulence Promoter P/D over a Reynolds Number Range $1.8 \times 10^4 \leq N_{Re} \leq 3.8 \times 10^4$.

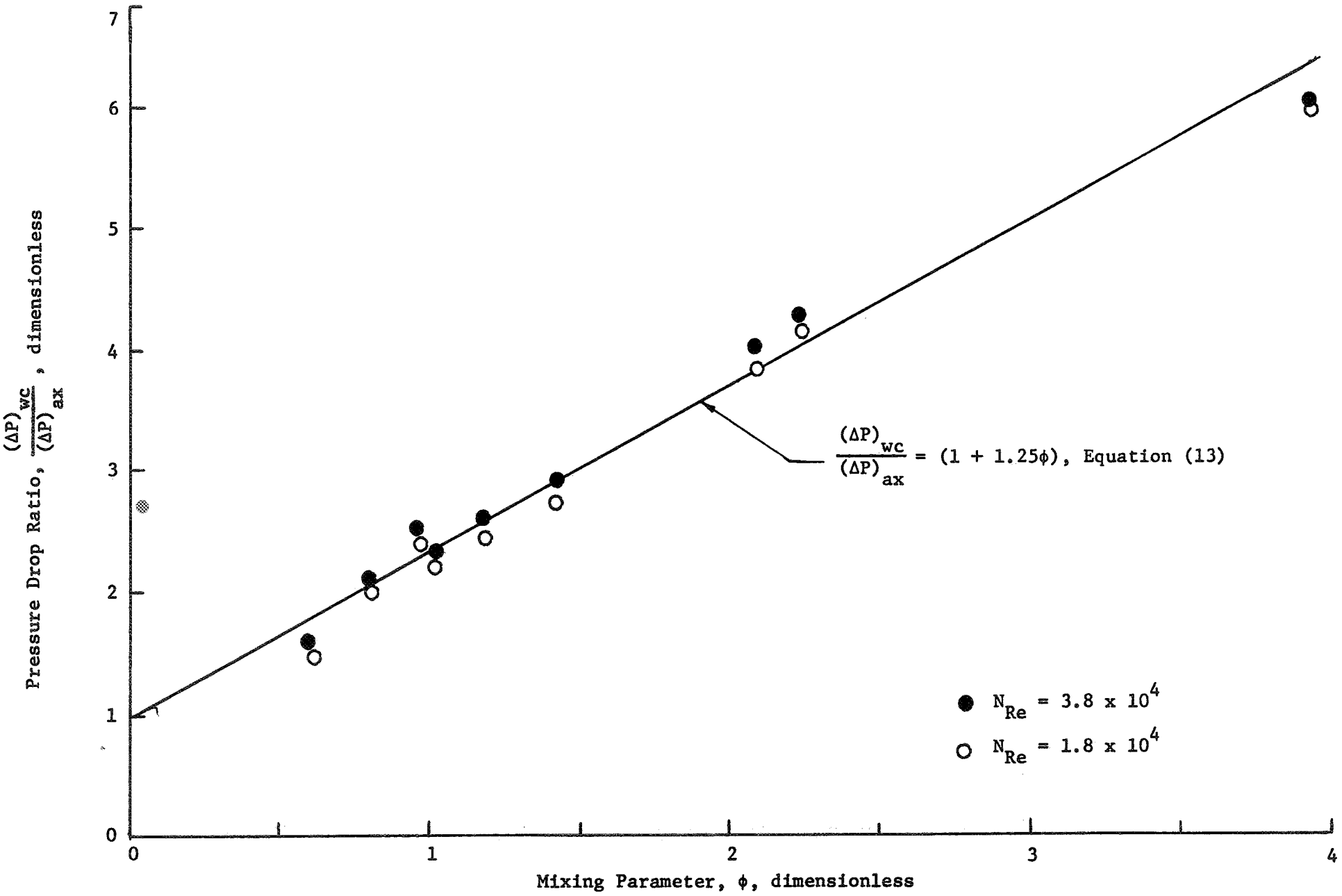

Figure 18. Pressure Drop Ratio, $(\Delta P)_{wc}/(\Delta P)_{ax}$ vs. Mixing Parameter ϕ over a Reynolds Number Range $1.8 \times 10^4 \leq N_{Re} \leq 3.8 \times 10^4$.

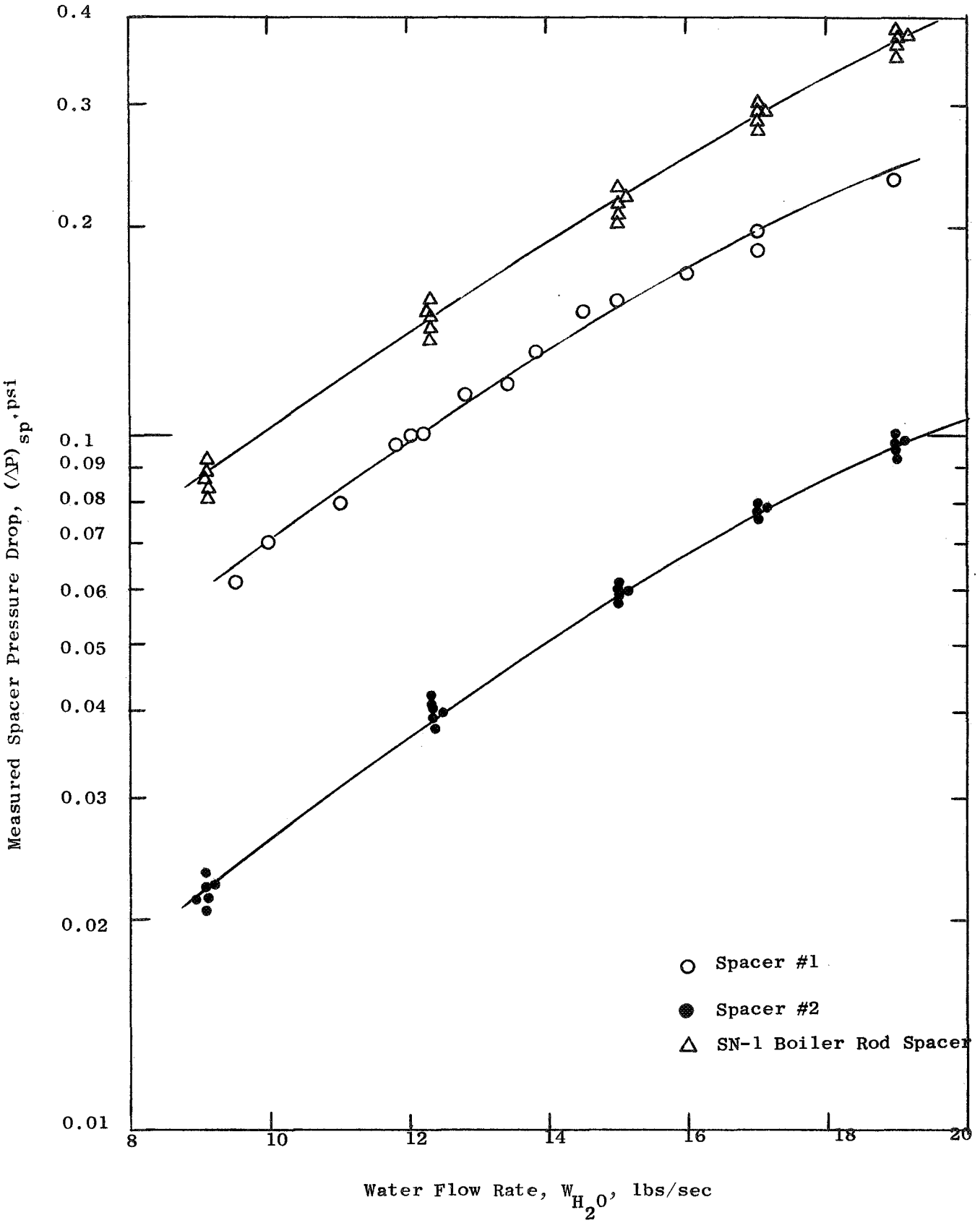

Figure 19. Measured Spacer Pressure Drop for the Case of Incoming Axial Flow.

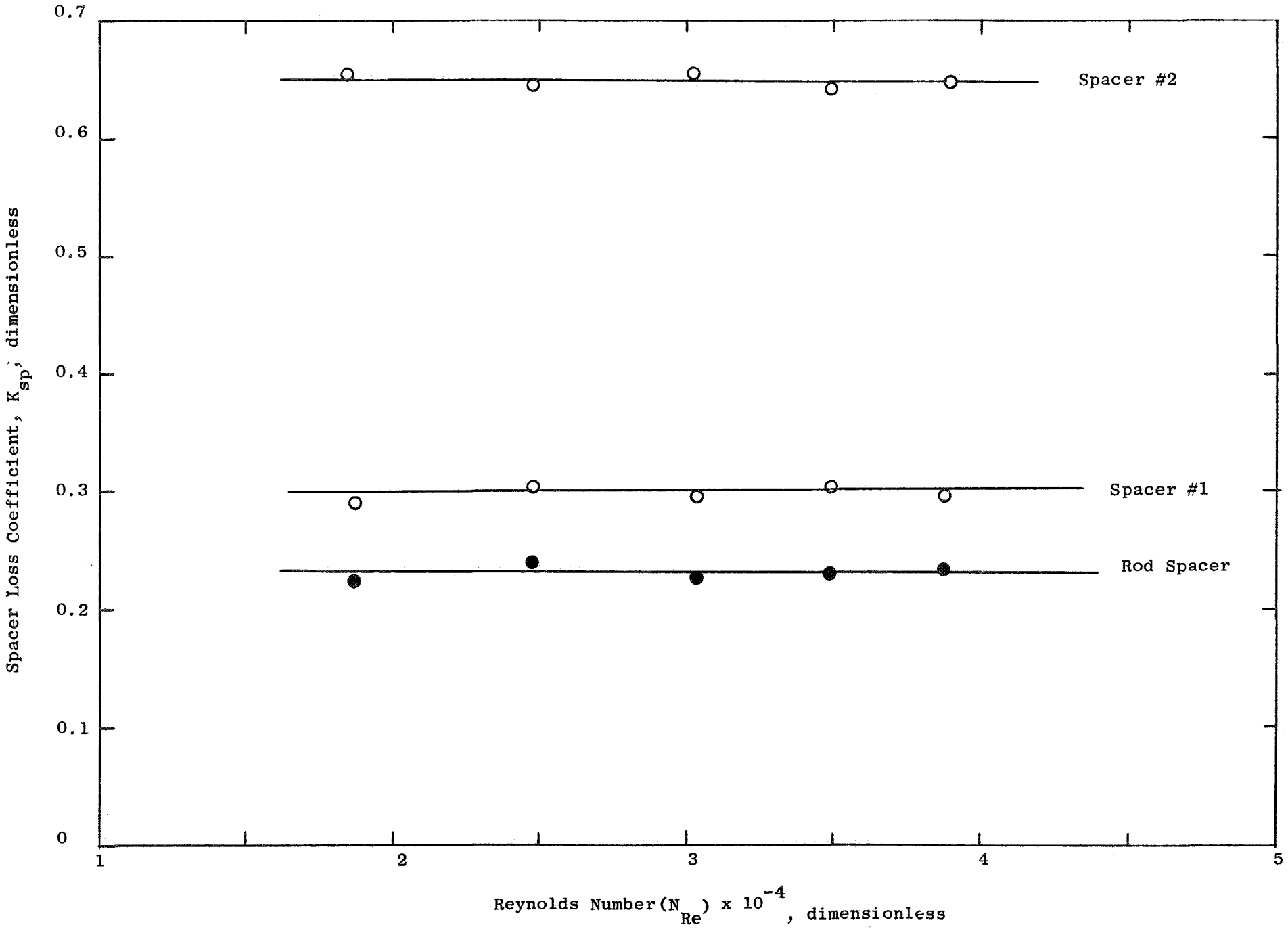

Figure 20. Spacer Loss Coefficient vs. Reynolds Number for the case of Incoming Axial Flow.

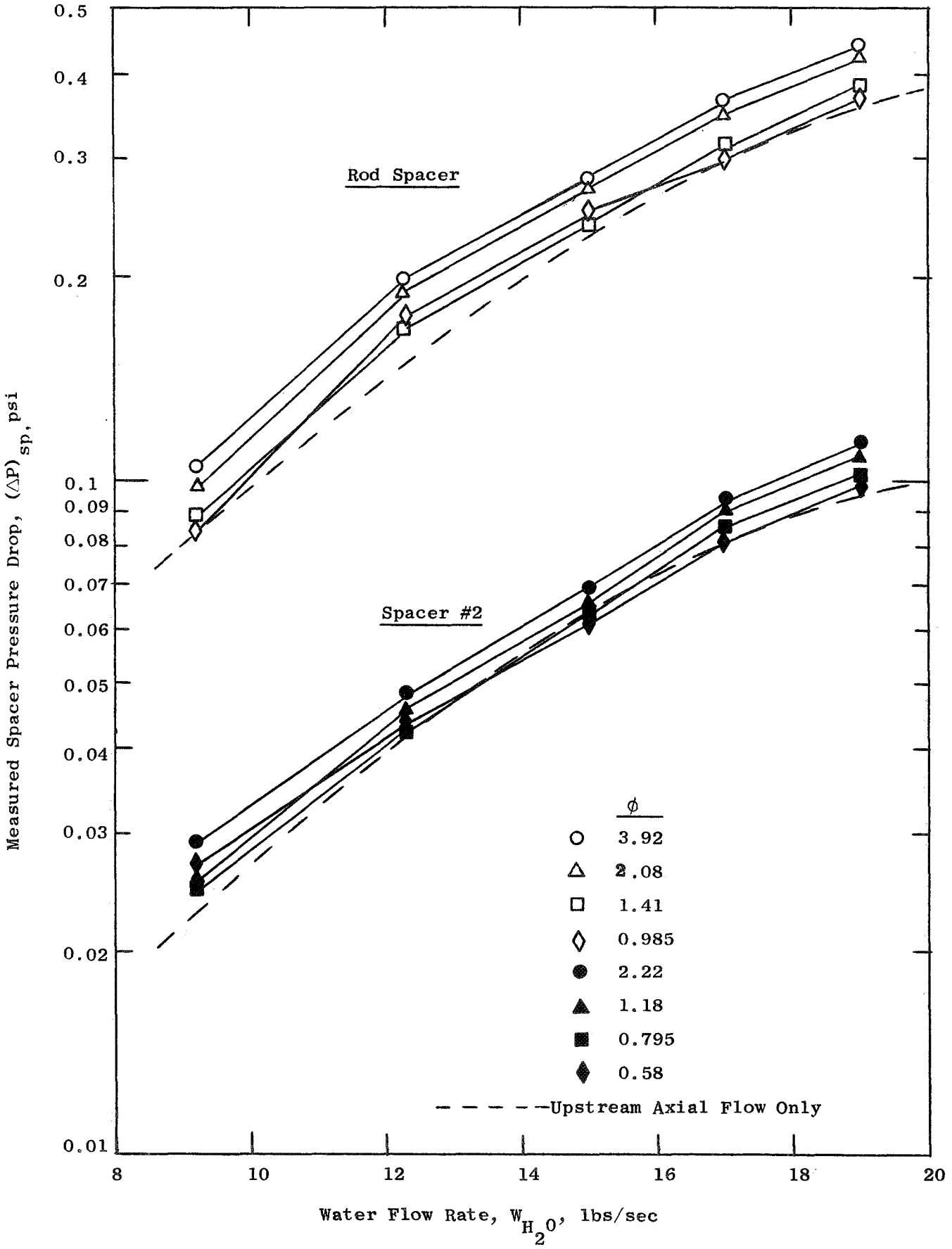

Figure 21. Measured Spacer Pressure Drop for the Case of Incoming Perturbed Axial Flow.

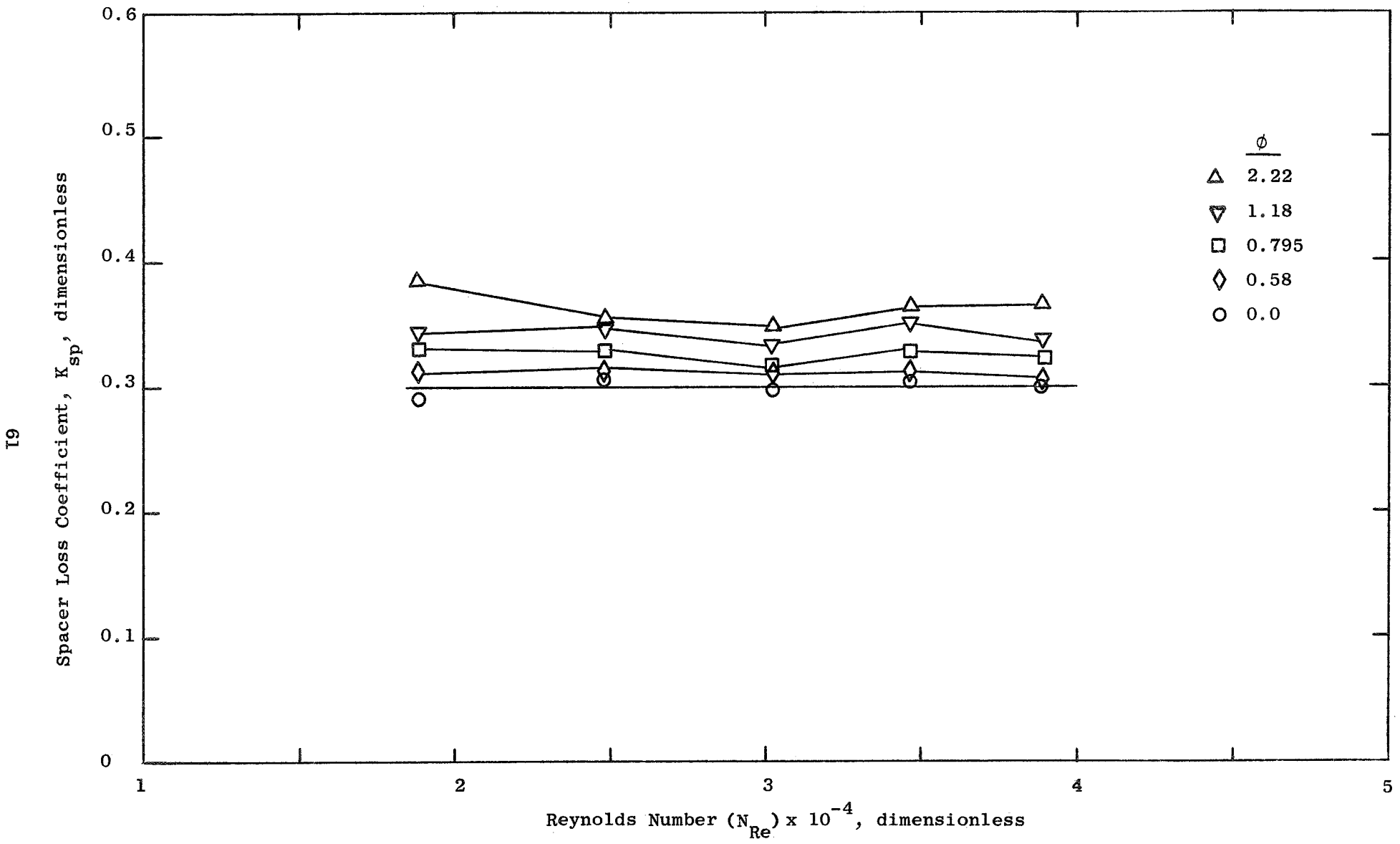

Figure 22. Effect of Incoming Flow Mixing Level on Spacer No. 2 Loss Coefficient.

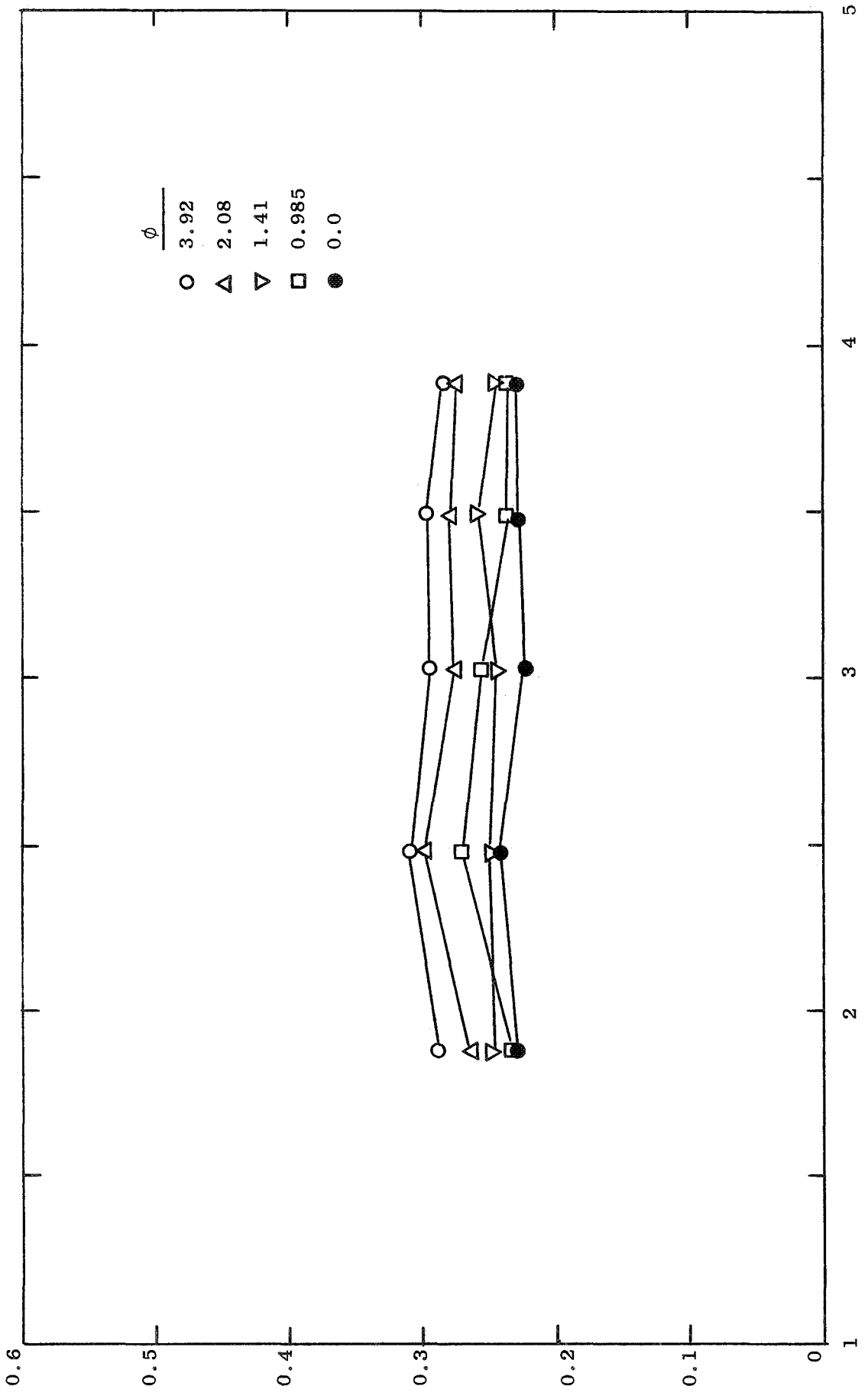

Figure 23. Effect of Incoming Flow Mixing Level on Rod Space Loss Coefficient.

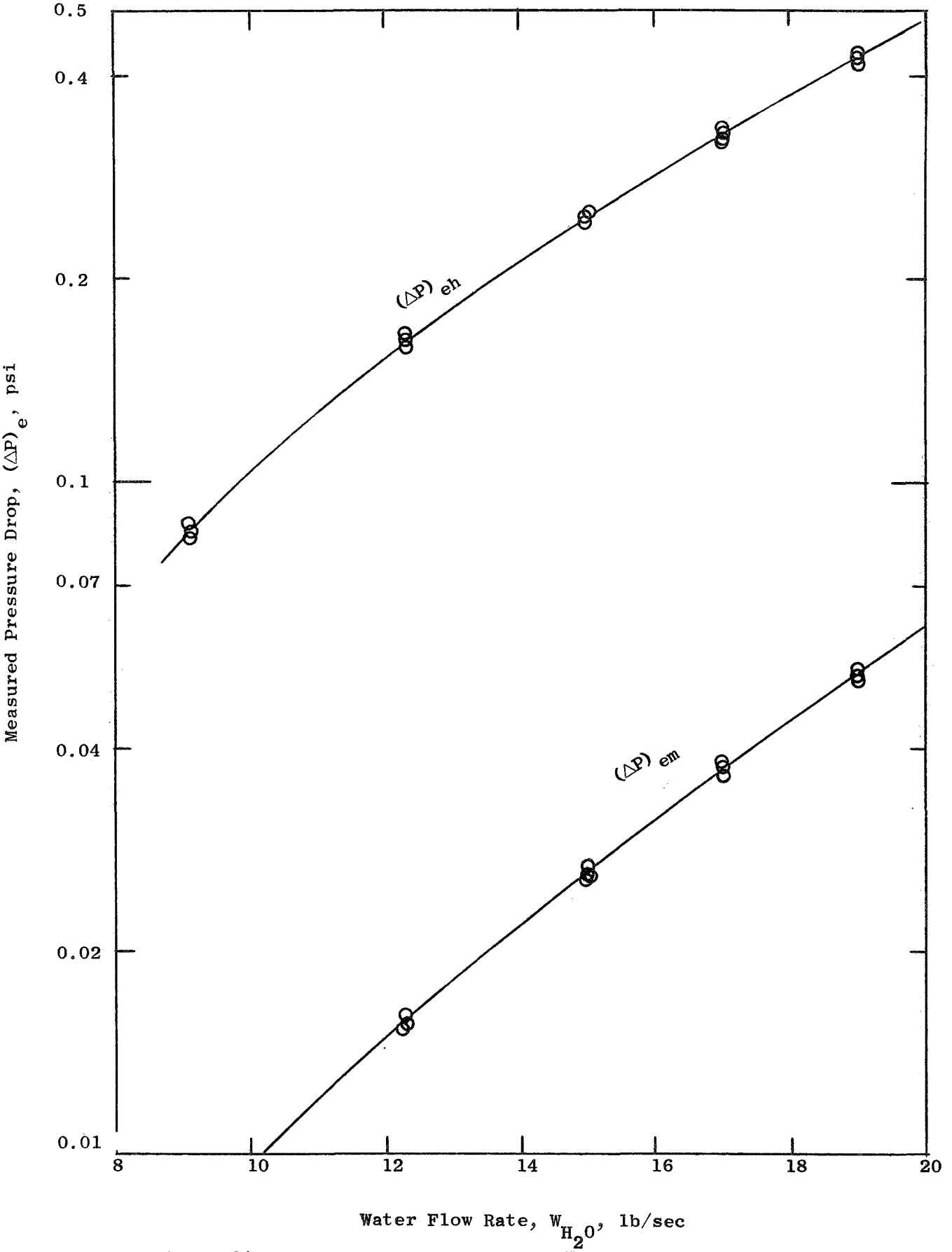

Figure 24. Measured Pressure Drop for the Exit Radial Ports and the Exit Manifold.

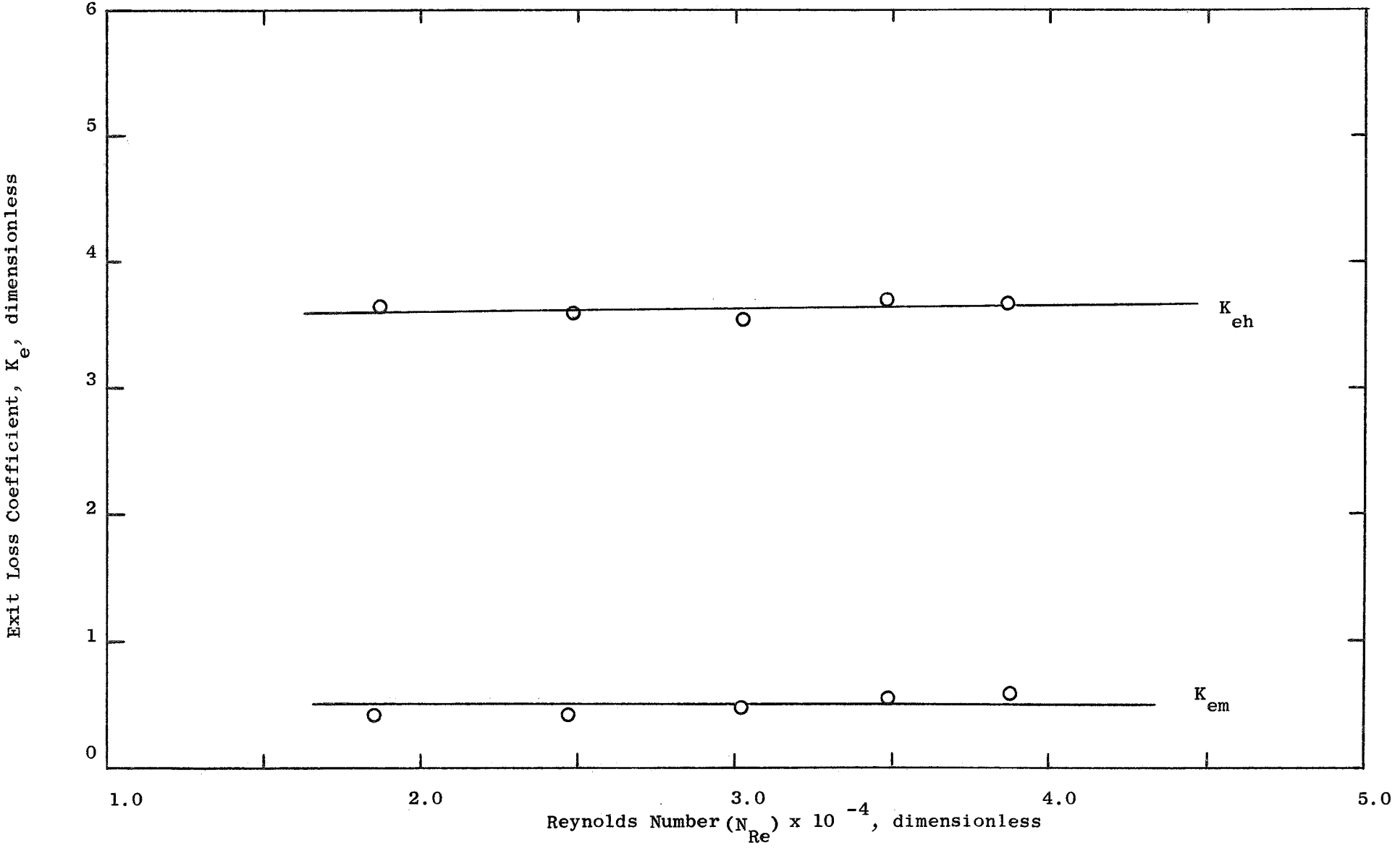

Figure 25. Measured Exit Loss Coefficient vs. Reynolds Number for the Radial Ports and Manifold.

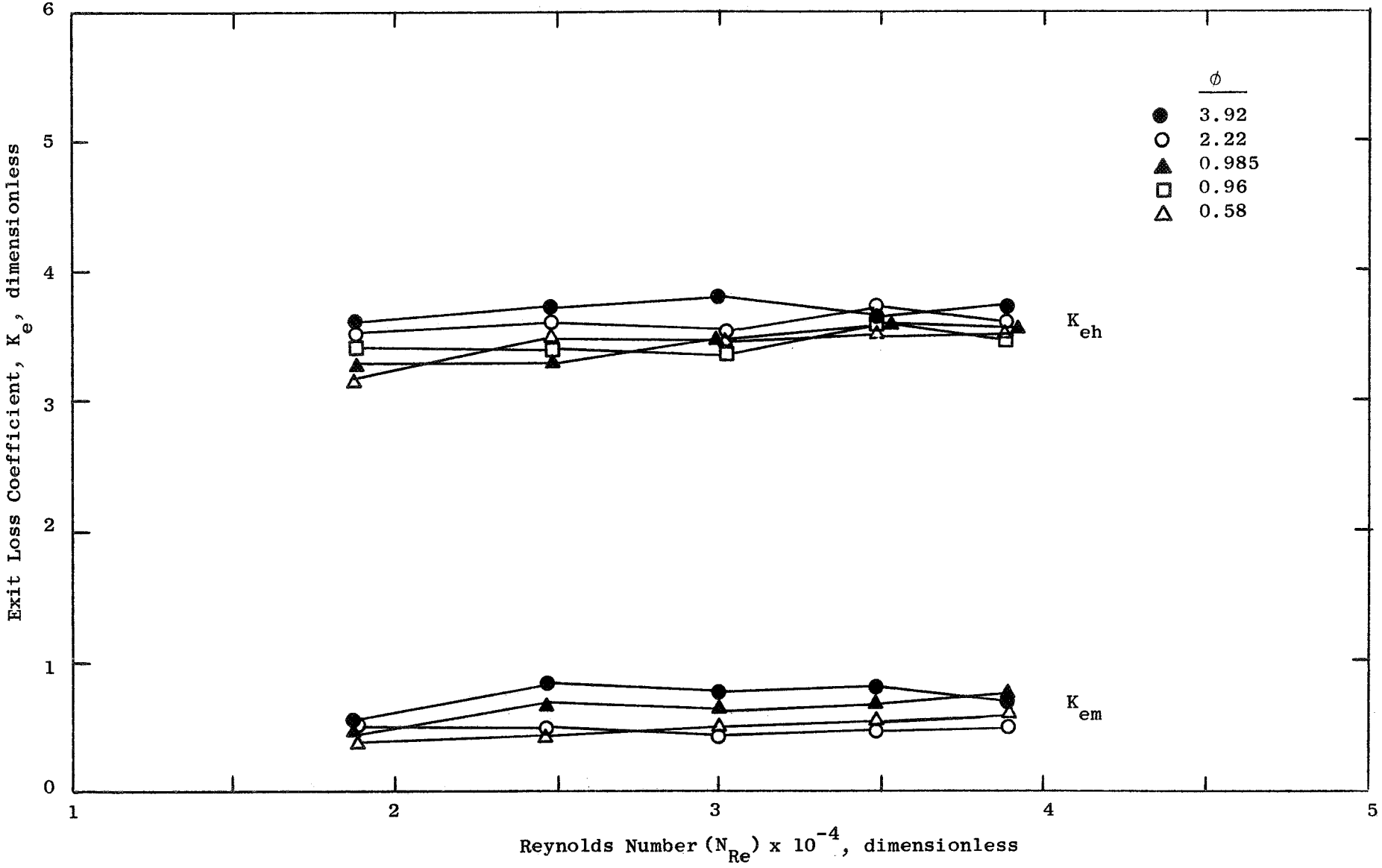

Figure 26. Effect of Upstream Flow Mixing Level on Exit Loss Coefficient.

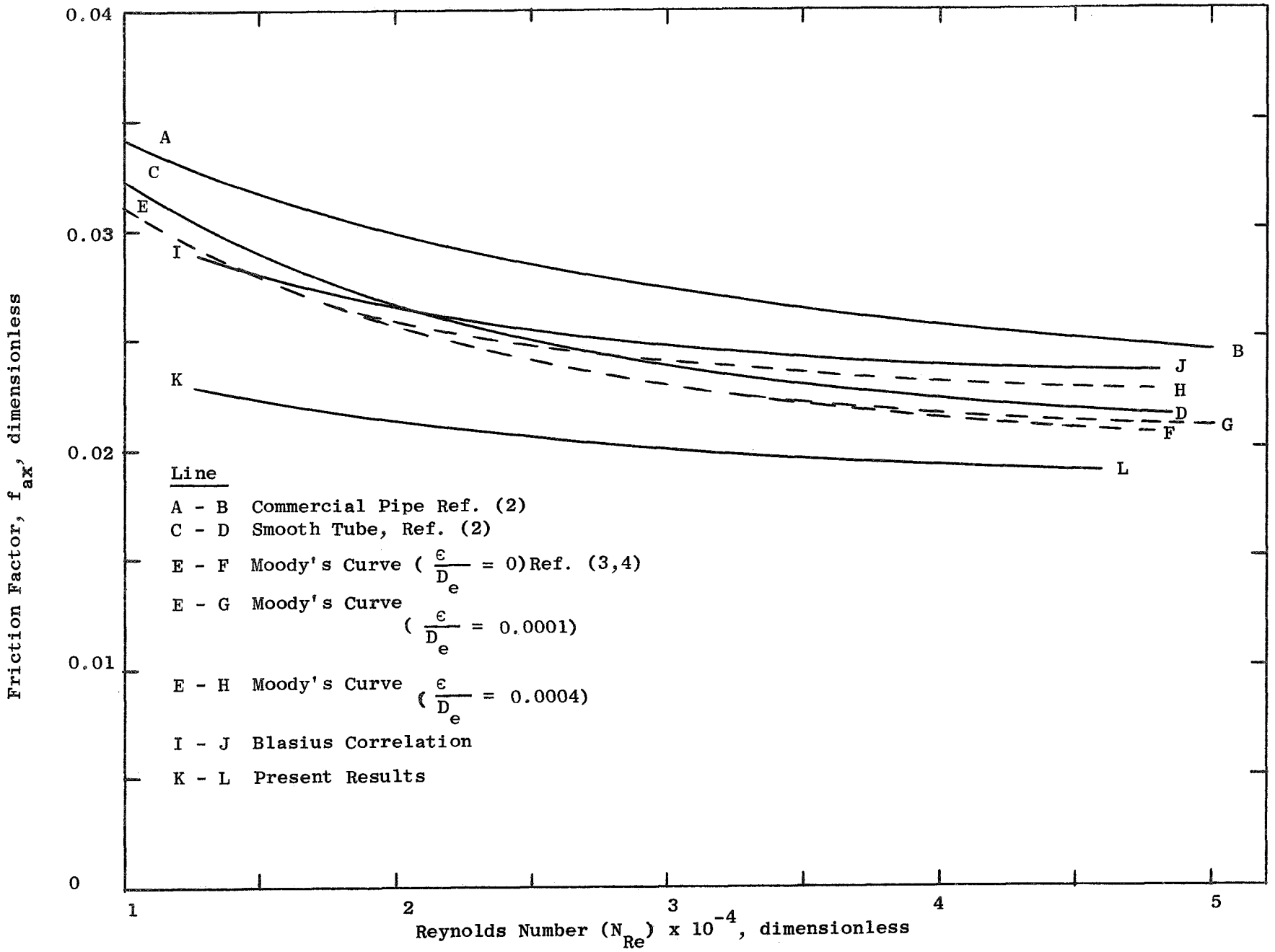

Figure 27. Comparison of Friction Factors Between Conventional Predictions and the Present Results.

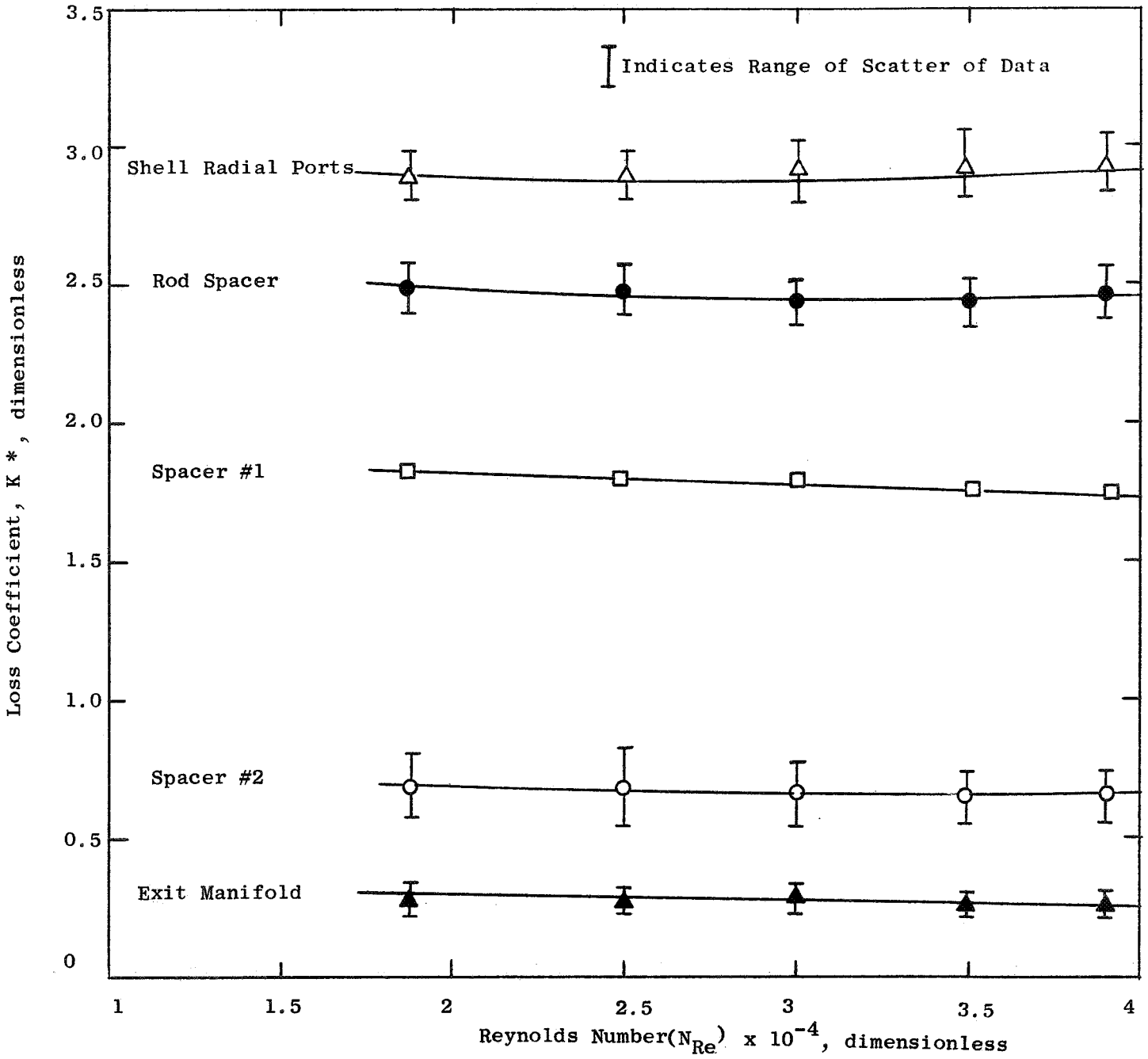

Figure 28. Comparison of Shell Side Flow Loss Coefficients (Based upon Shell Side Velocity Head)

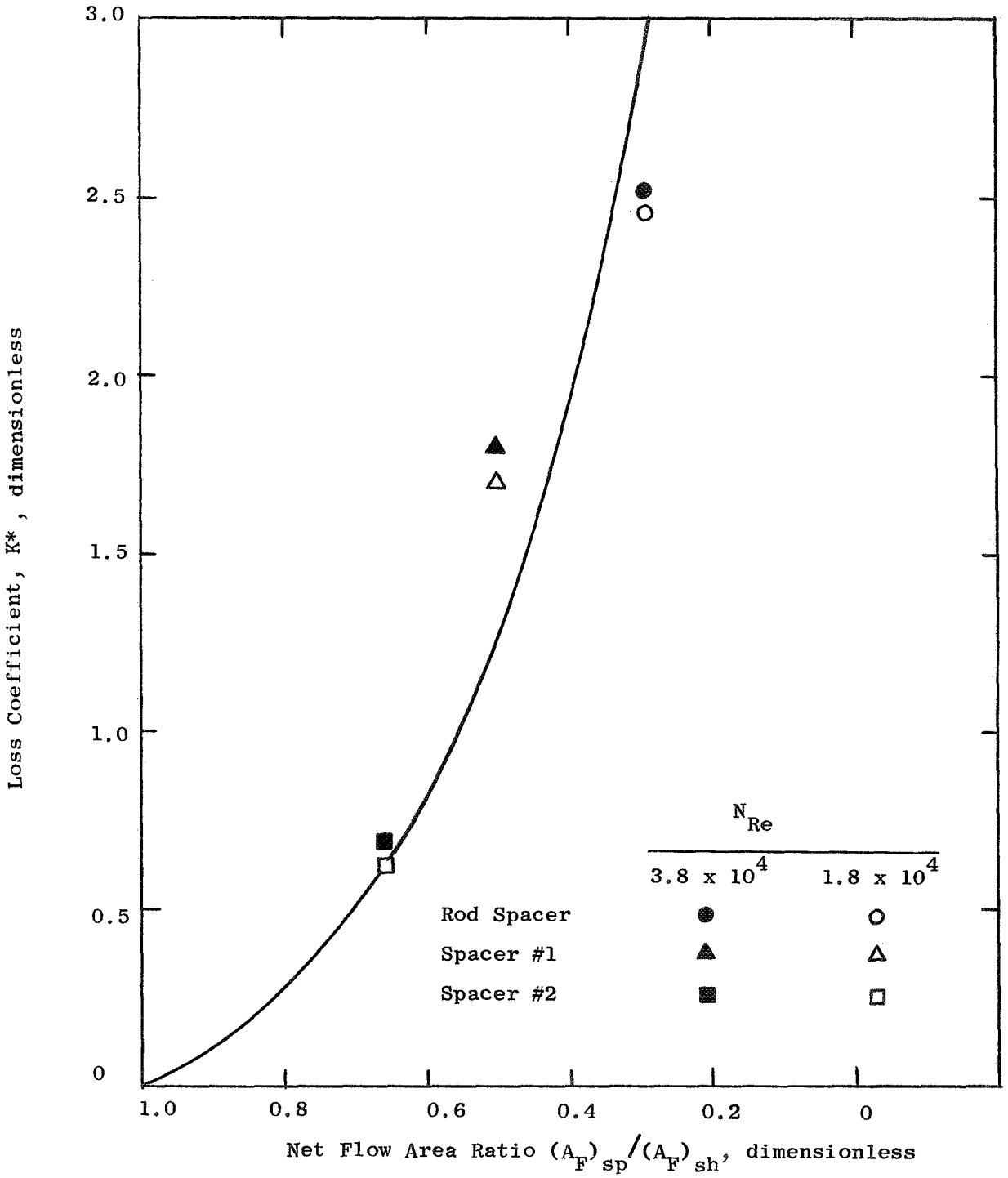

Figure 29. Spacer Loss Coefficients (Based upon Shell Side Velocity Head) vs. Area Ratio Over a Reynolds Number Range of $1.8 \times 10^4 \leq N_{Re} \leq 3.8 \times 10^4$.

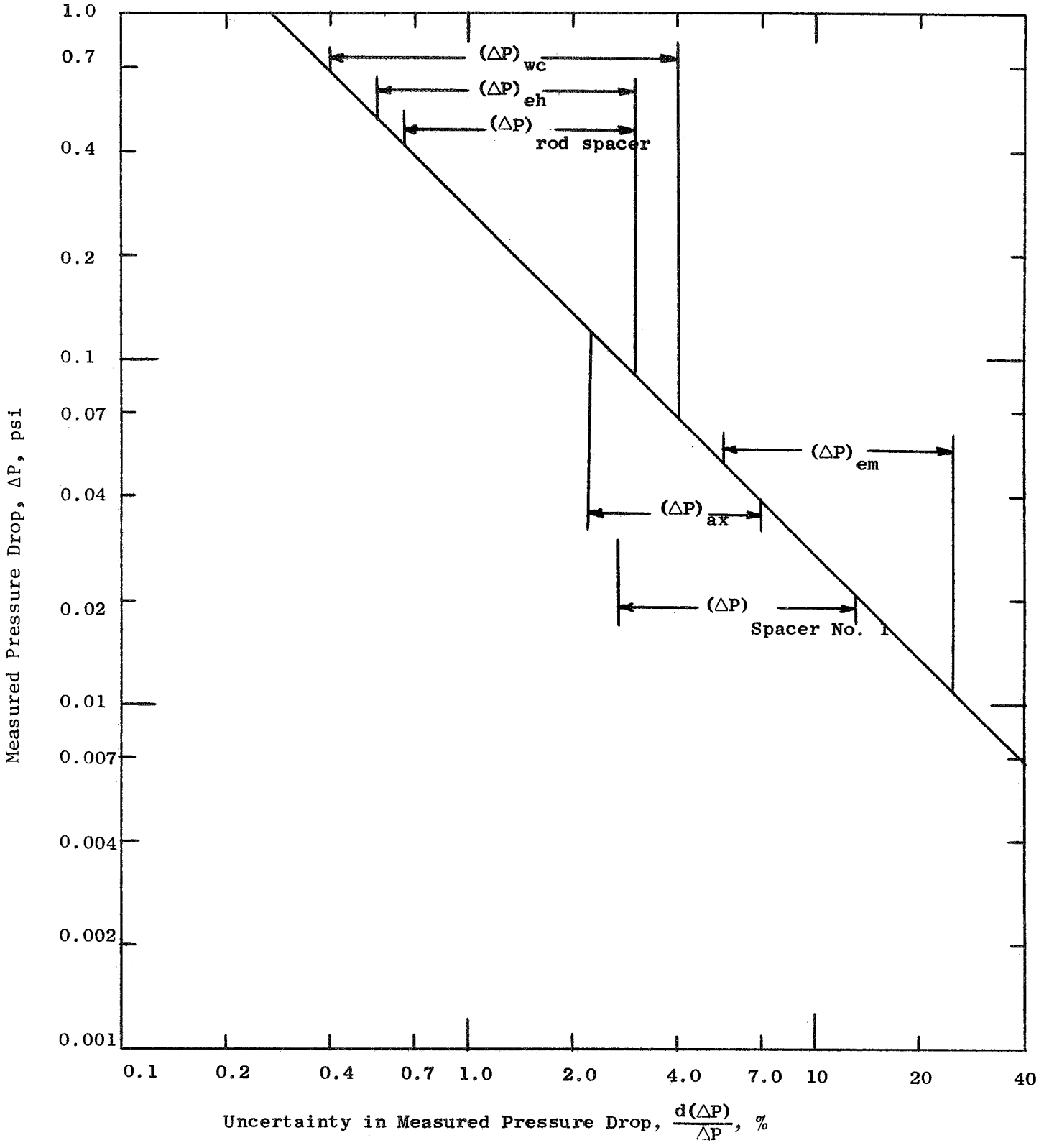

Figure 30. Error Analysis Curve Range of Uncertainty for Various Measured Pressure Drops.

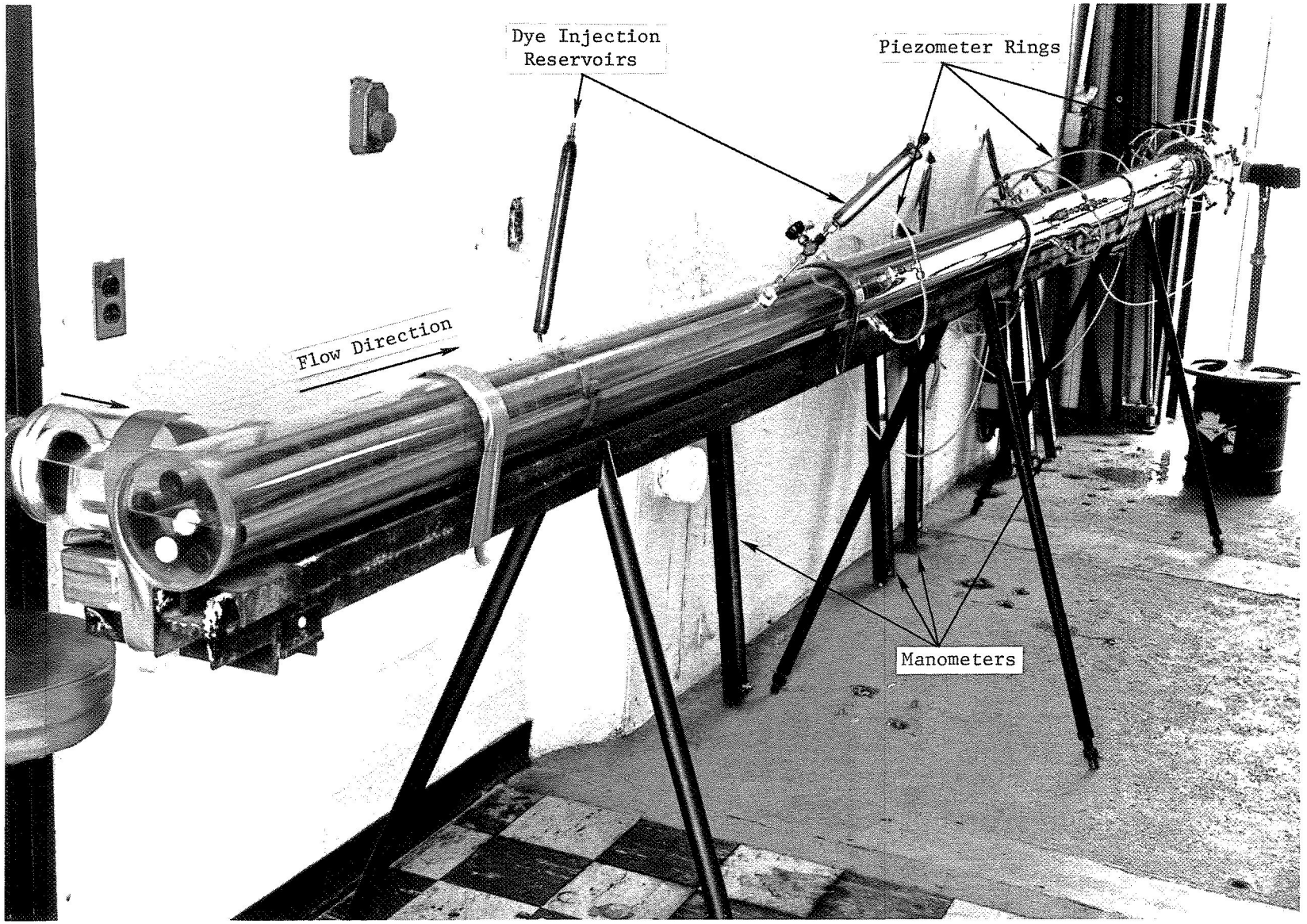

Figure 31. Photographic View of the Shell Side Hydraulic Test Setup. (Inlet Region) (69-3-34K)

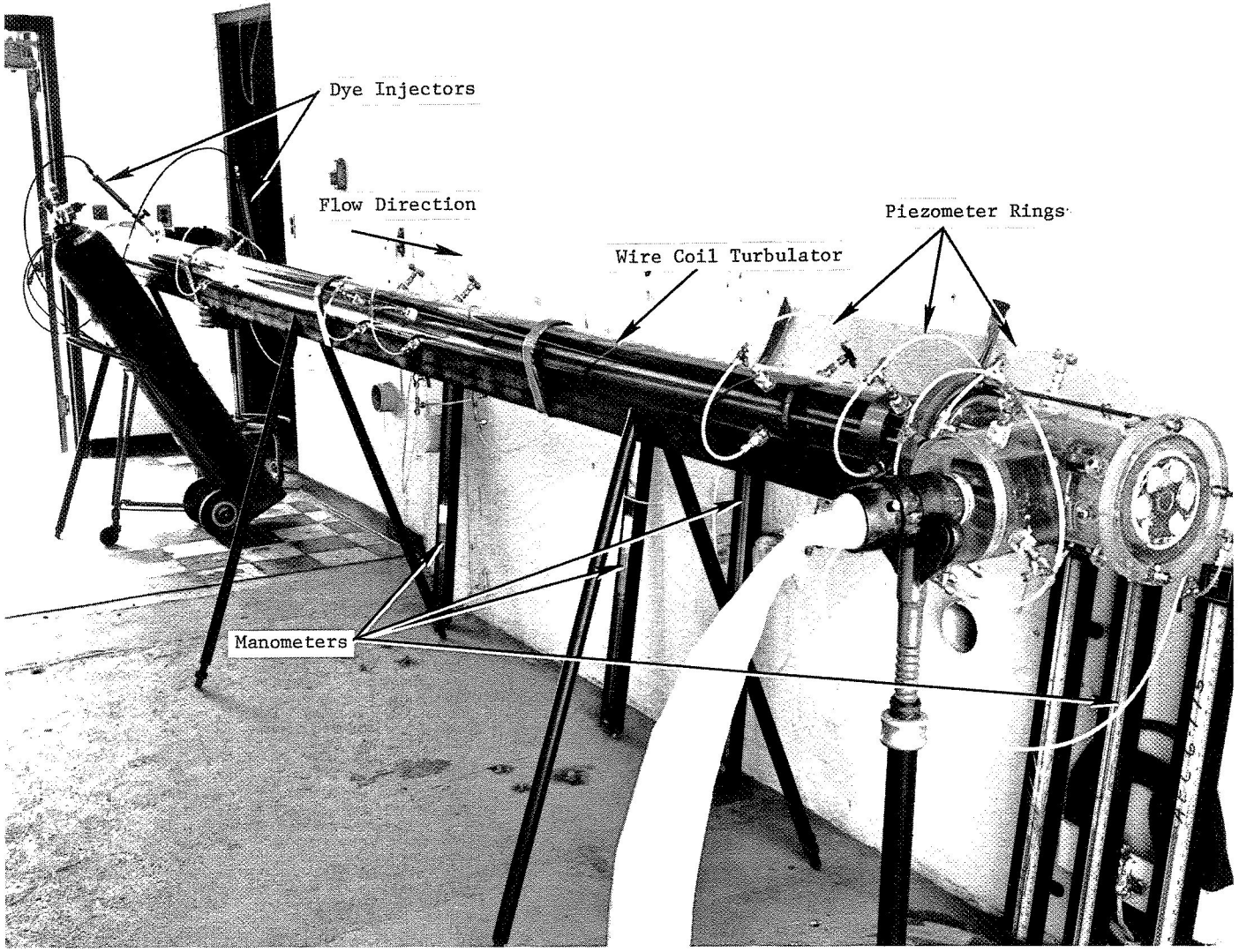

Figure 32. Photographic View of SNAP-8 Boiler Shell-Side Hydraulic Test. (Exit Region) (69-3-34J)

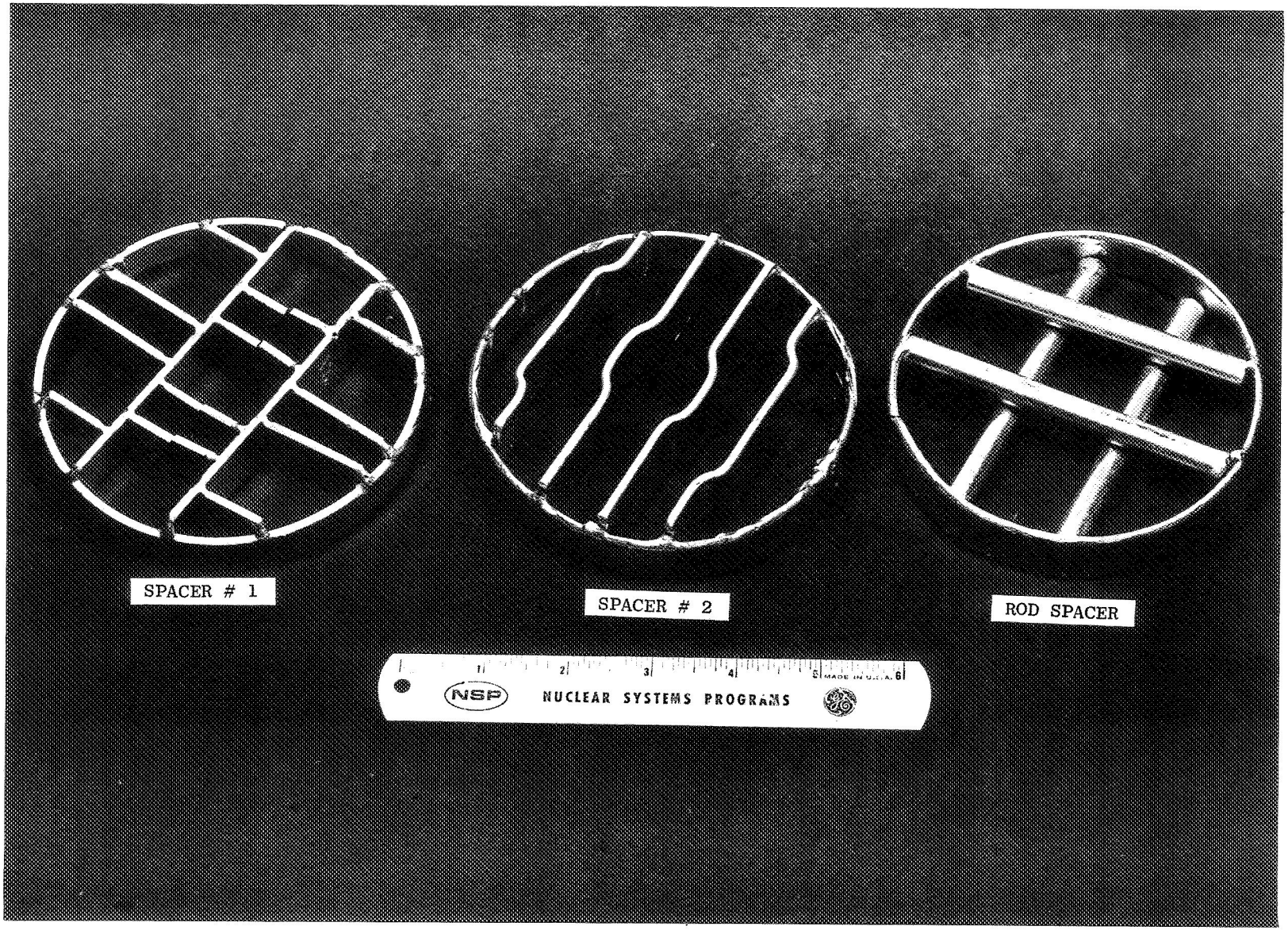

Figure 33. Photographic View of the Tube Supporting Spacers. (69-3-34L)

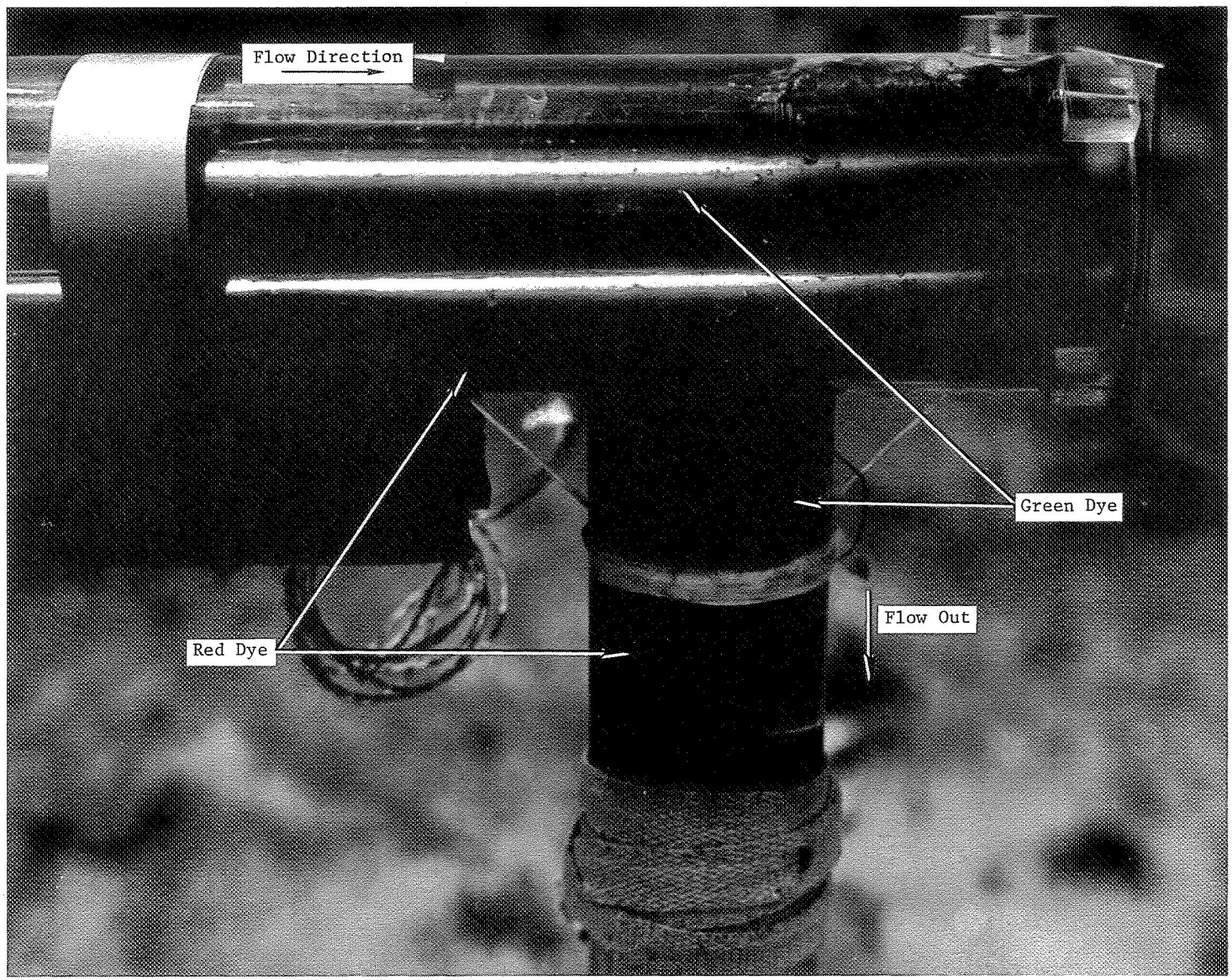

Figure 34. Illustration of Poor Mixing of Shell Side Flow in the Exit Region. (C11399)

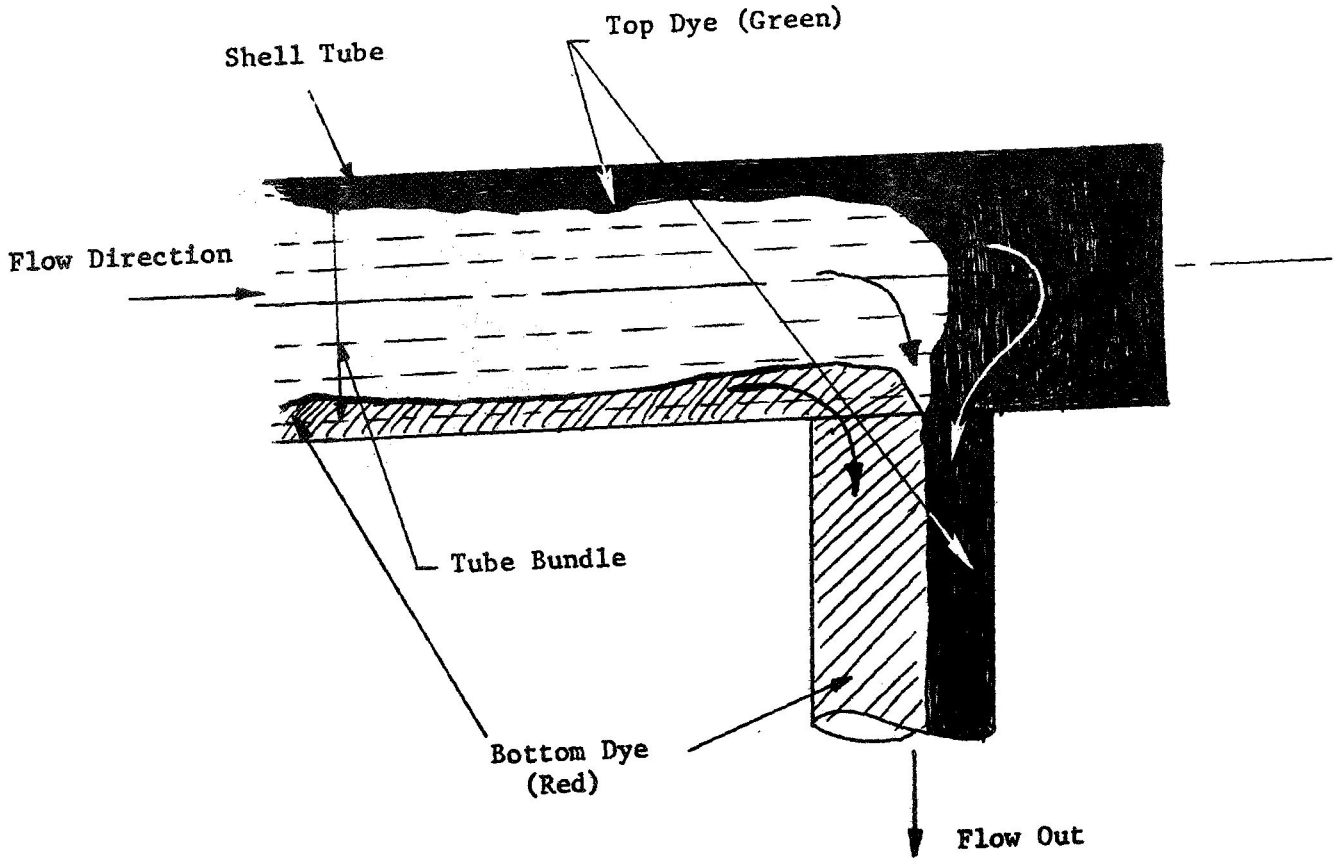

Figure 34a. Illustration of Poor Mixing of Shell Side Flow in the Exit Region (Depicted from color photo CDC-11399)

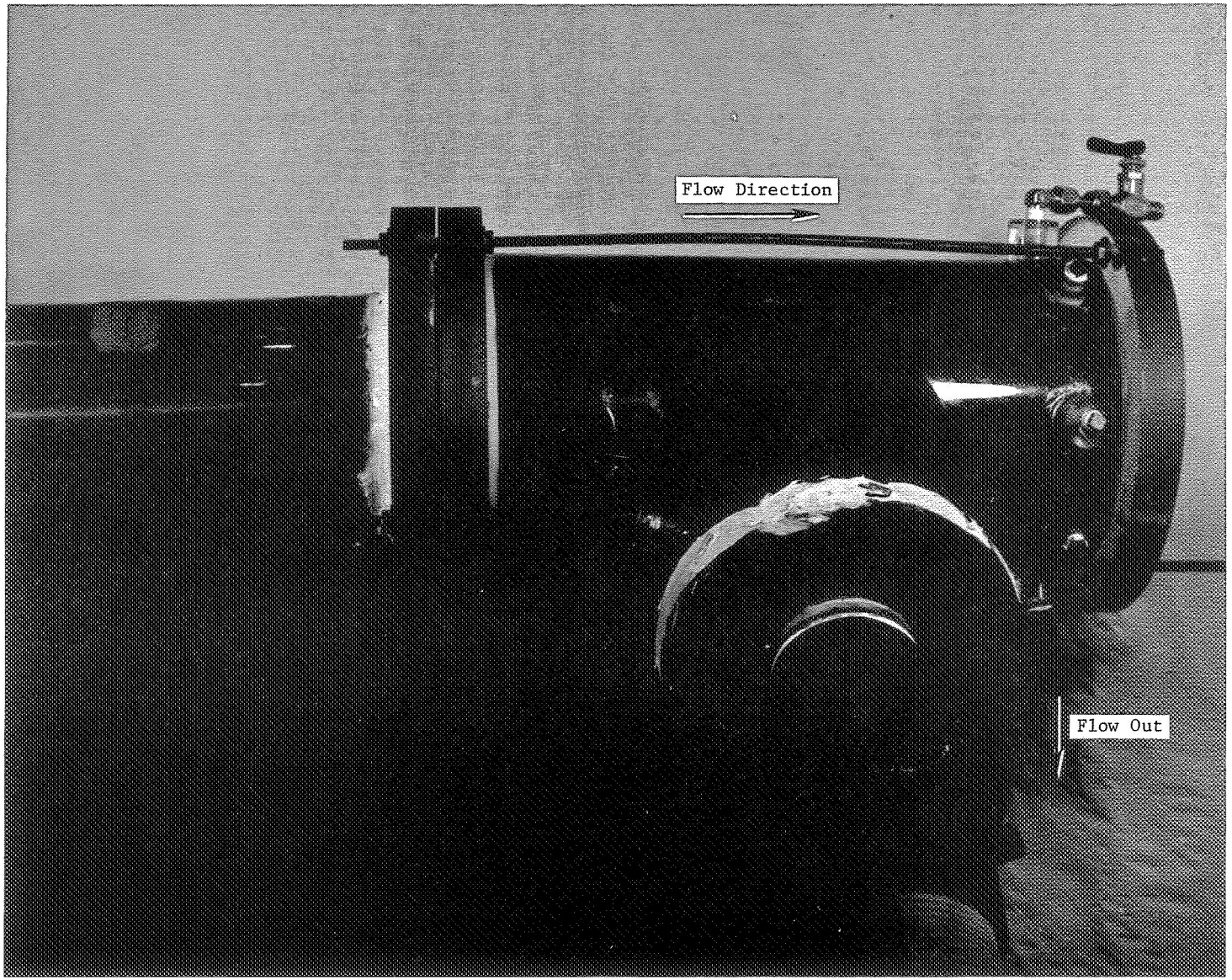

Figure 35. Illustration of Good Mixing of Shell Side Flow in the Exit Region by Adding an Exit Manifold with Radial Ports in the Shell Tube. (69-2-33C)

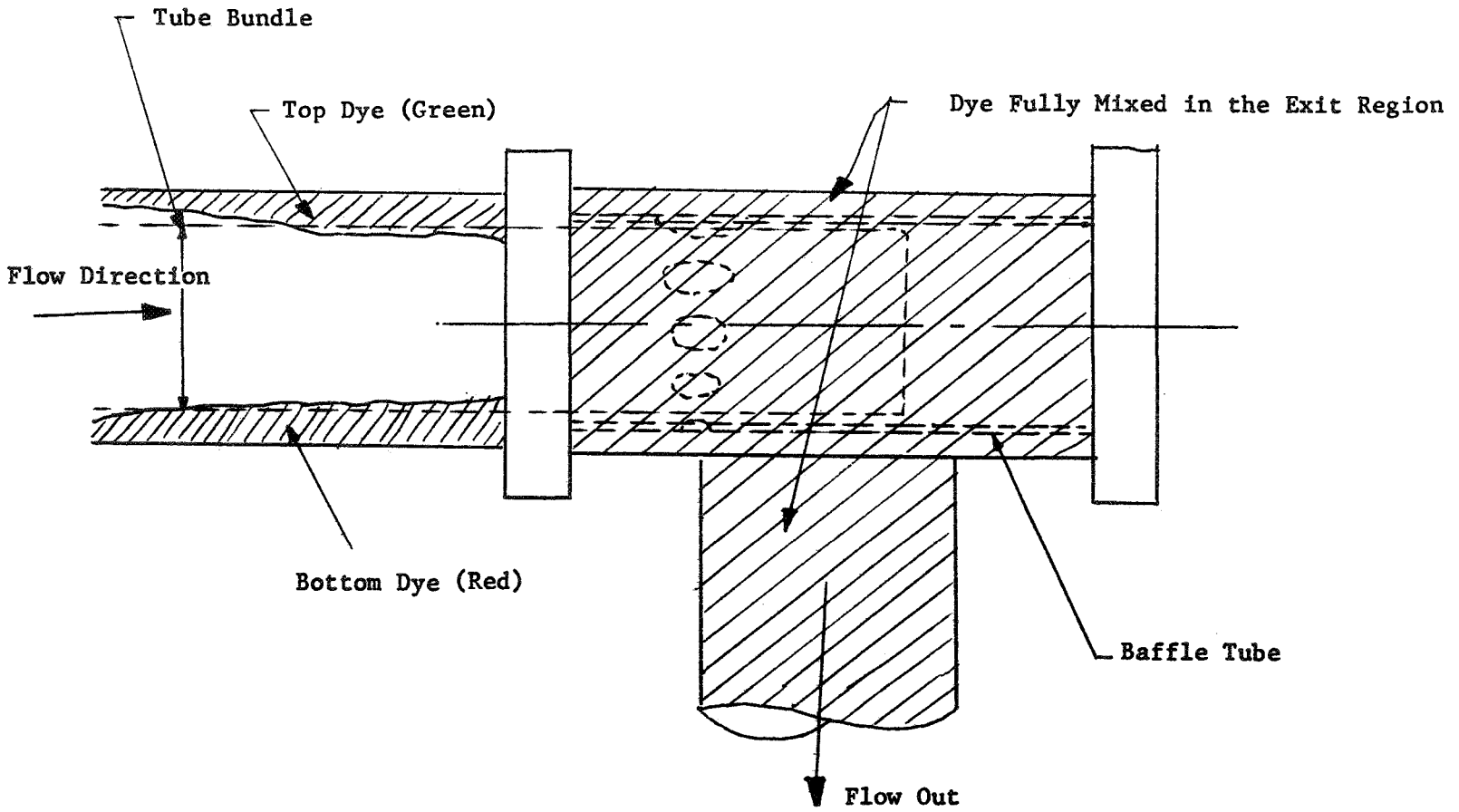

Figure 35a. Illustration of Good Mixing of Shell Side Flow in the Exit Region by Adding an Exit Manifold with Radial Ports in the Baffle Tube. (Depicted from color photo 69-2-33C)

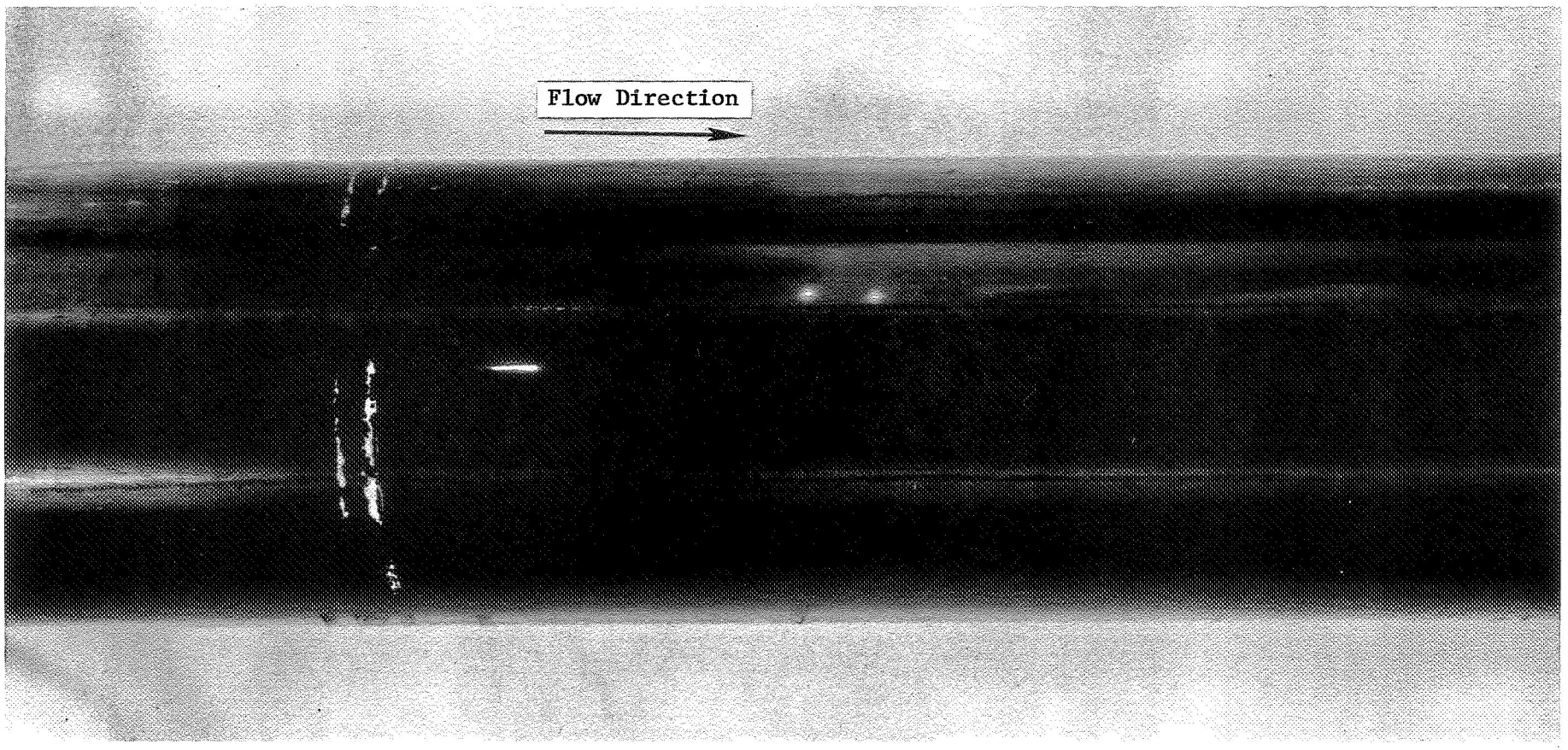

Figure 36. Illustration of Poor Mixing of Shell Side Flow Passing Through Tube Bundle. (69-2-33E)

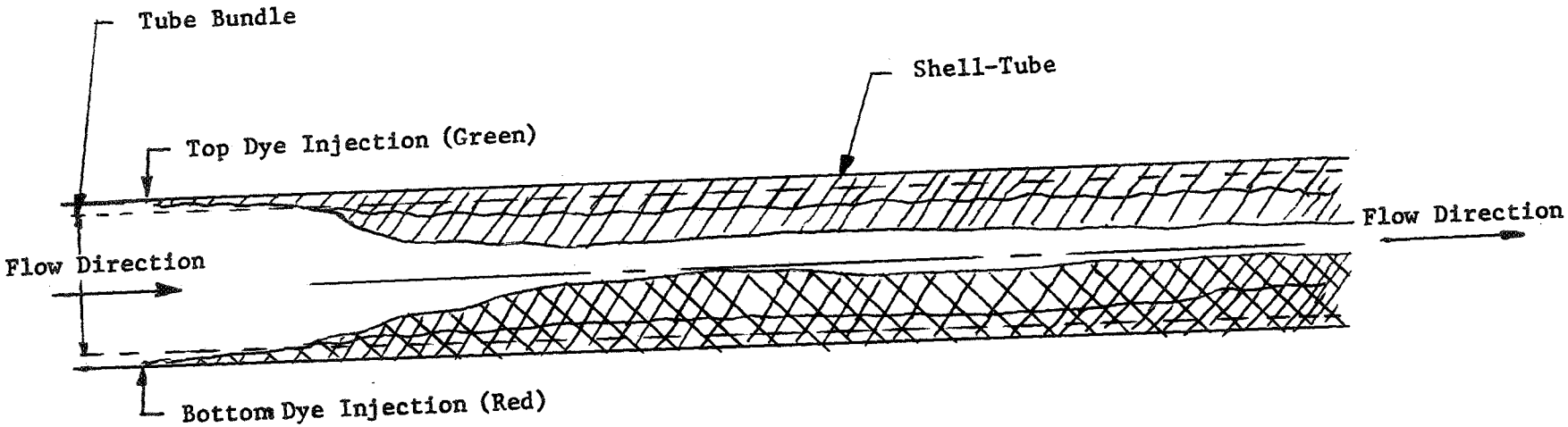

Figure 36a. Illustration of Poor Mixing of Shell Side Flow Passing Through Tube Bundle (Depicted from color photo 69-2-33E)

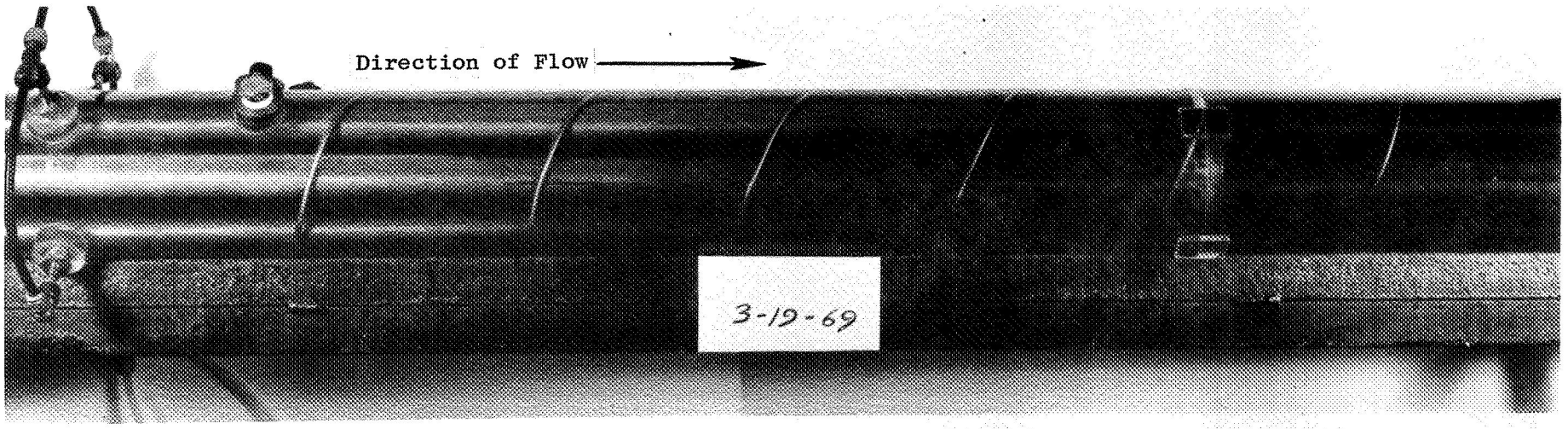

Figure 37. Illustration of Good Mixing of Shell Side Flow by Adding Turbulence Promoter (3/16" x 6" Wire Coil). (69-3-34E)

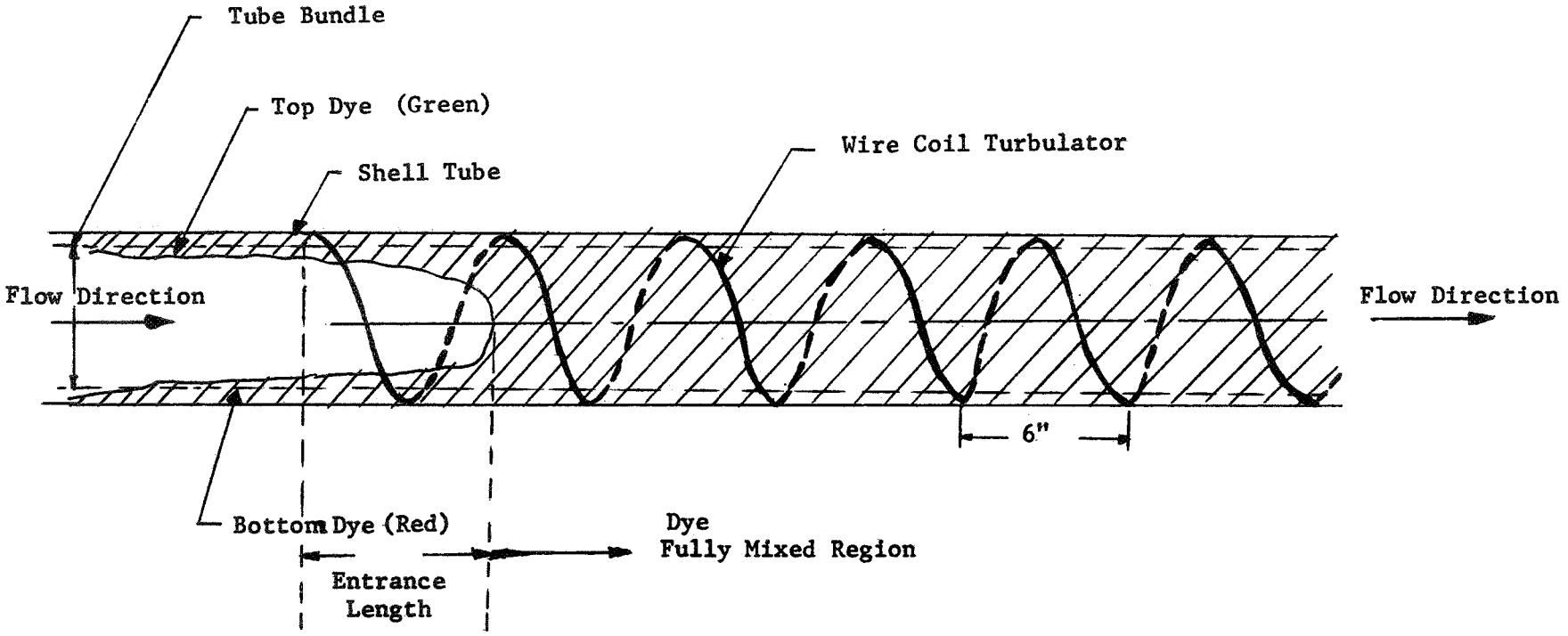

Figure 37a. Illustration of Good Mixing of Shell-Side Flow by Adding Turbulence Promoter (3/16" x 6" Wire Coil). Also Illustrating the Length Required for Fully Developed Mixing. (Depicted from color photo 69-3-34E)

DISTRIBUTION LIST
TOPICAL REPORT
CONTRACT NAS 3-10610

NASA
Washington, D.C. 20546
Attn: P. R. Miller (RNP)

NASA
Washington, D.C. 20546
Attn: James J. Lynch (RNP)

NASA
Washington, D.C. 20546
Attn: George C. Deutsch (RR)

NASA
Washington, D.C. 20546
Attn: Dr. Fred Schulman (RNP)

NASA
Washington, D.C. 20546
Attn: H. Rochen (RNP)

NASA
Scientific and Tech. Info. Facility
P.O. Box 33
College Park, Maryland 20740
Attn: Acquisitions Branch
(SQT - 34054) 2 Copies

NASA
Ames Research Center
Moffett Field, California 94035
Attn: Librarian

NASA
Goddard Space Flight Center
Greenbelt, Maryland 20771
Attn: Librarian

NASA
Langley Research Center
Hampton, Virginia 23365
Attn: Librarian

NASA
Manned Spacecraft Center
Houston, Texas 77001
Attn: Librarian

NASA
George C. Marshall Space Flight Ctr.
Huntsville, Alabama 35812
Attn: Librarian

NASA
Jet Propulsion Laboratory
4800 Oak Grove Drive
Pasadena, California 91103
Attn: Librarian

NASA
Lewis Research Center
21000 Brookpark Road
Cleveland, Ohio 44135
Attn: Librarian

NASA
Lewis Research Center
21000 Brookpark Road
Cleveland, Ohio 44135
Attn: H. O. Slone, MS 500-201

NASA
Lewis Research Center
21000 Brookpark Road
Cleveland, Ohio 44135
Attn: G. M. Ault, MS 105-1

NASA
Lewis Research Center
21000 Brookpark Road
Cleveland, Ohio 44135
Attn: P. L. Stone, MS 106-1

NASA
Lewis Research Center
21000 Brookpark Road
Cleveland, Ohio 44135
Attn: G. M. Thur, MS 500-202

NASA
Lewis Research Center
21000 Brookpark Road
Cleveland, Ohio 44135
Attn: John E. Dilley, MS 500-309

NASA
Lewis Research Center
21000 Brookpark Road
Cleveland, Ohio 44135
Attn: Technology Utilization, MS 3-19

NASA
Lewis Research Center
21000 Brookpark Road
Cleveland, Ohio 44135
Attn: Report Control Office, MS 5-5

NASA
Lewis Research Center
21000 Brookpark Road
Cleveland, Ohio 44135
Attn: R. L. Davies, MS 106-1

NASA
Lewis Research Center
21000 Brookpark Road
Cleveland, Ohio 44135
Attn: V. F. Hlavin, MS 3-14
(Final Only)

NASA
Lewis Research Center
21000 Brookpark Road
Cleveland, Ohio 44135
Attn: E. R. Furman, MS 500-202
3 Copies

NASA
Lewis Research Center
21000 Brookpark Road
Cleveland, Ohio 44135
Attn: M. J. Saari, MS 500-202

NASA
Lewis Research Center
21000 Brookpark Road
Cleveland, Ohio 44135
Attn: R. English, MS 500-201

NASA
Lewis Research Center
21000 Brookpark Road
Cleveland, Ohio 44135
Attn: M. Gutstein, MS 500-201

National Bureau of Standards
Washington, D.C. 20546
Attn: Librarian

AFSC
Aeronautical Systems Division
Wright-Patterson AFB, Ohio 45433
Attn: Charles Armbruster (ASRPP-10)

AFSC
Aeronautical Systems Division
Wright-Patterson AFB, Ohio 45433
Attn: T. Cooper

AFSC
Aeronautical Systems Division
Wright-Patterson AFB, Ohio 45433
Attn: Librarian

Army Ordnance Frankford Arsenal
Bridesburg Station
Philadelphia, Pennsylvania 19137
Attn: Librarian

U.S. Atomic Energy Commission
Tech. Info. Service Extension
P.O. Box 62
Oak Ridge, Tennessee 37831

U.S. Atomic Energy Commission
Washington, D.C. 20545
Attn: M. J. Whitman

U.S. Atomic Energy Commission
Washington, D.C. 20545
Attn: J. M. Simmons

Argonne National Laboratory
9700 South Cass Avenue
Argonne, Illinois 60440
Attn: Librarian

Battelle Memorial Institute
505 King Avenue
Columbus, Ohio 43201
Attn: R. T. Nichoff, DMIC

Battelle Memorial Institute
505 King Avenue
Columbus, Ohio 43201
Attn: Librarian

Brookhaven National Laboratory
Upton, Long Island, New York, 11973
Attn: Librarian

Brookhaven National Laboratory
Upton, Long Island, New York 11973
Attn: Dr. D. H. Gurinsky

Brookhaven National Laboratory
Upton, Long Island, New York 11973
Attn: Dr. J. R. Weeks

Oak Ridge National Laboratory
Oak Ridge, Tennessee 37831
Attn: J. Devan

Oak Ridge National Laboratory
Oak Ridge, Tennessee 37831
Attn: R. MacPherson

Oak Ridge National Laboratory
Oak Ridge, Tennessee 37831
Attn: Librarian

Office of Naval Research
Power Division
Washington, D.C. 20360
Attn: Librarian

Bureau of Weapons
Research and Engineering
Materials Division
Washington, D.C. 20546
Attn: Librarian

U.S. Naval Research Laboratory
Washington, D.C. 20390
Attn: Librarian

Aerojet-General Corporation
Electronics Division
Azusa, California 91703
Attn: Librarian

AiResearch Manufacturing Company
Division of the Garrett Corporation
Sky Harbor Airport
402 South 36th Street
Phoenix, Arizona 85034
Attn: Librarian

AiResearch Manufacturing Company
Division of the Garrett Corporation
9851-9951 Sepulveda Boulevard
Los Angeles, California 90009
Attn: Librarian

IIT Research Institute
10 West 35th Street
Chicago, Illinois 60616
Attn: Librarian

Babcock & Wilcox Company
Research Center
Alliance, Ohio 44601
Attn: Librarian

North American Rockwell Corporation
Atomics International Division
8900 DeSoto Avenue
Canoga Park, California 91304
Attn: Librarian

North American Rockwell Corporation
Atomics International Division
8900 DeSoto Avenue
Canoga Park, California 91304
Attn: P. B. Ferry

North American Rockwell Corporation
Atomics International Division
8900 DeSoto Avenue
Canoga Park, California 91304
Attn: T. A. Moss

AVCO
Research & Advanced Development Dept.
201 Lowell Street
Wilmington, Massachusetts 01887
Attn: Librarian

Electro-Optical Systems, Inc.
Advanced Power Systems Division
Pasadena, California 91107
Attn: Librarian

Fansteel Metallurgical Corporation
North Chicago, Illinois 18201
Attn: Librarian

General Dynamics Corporation
General Atomic Division
John Jay Hopkins Lab.
P.O. Box 608
San Diego, California 92112
Attn: Librarian

General Electric Company
Space Division
3198 Chestnut Street
Philadelphia, Pennsylvania 19104
Attn: Librarian

General Electric Company
Vallecitos Atomic Laboratory
Pleasanton, California 94566
Attn: Librarian

General Dynamics/Fort Worth
P.O. Box 748
Fort Worth, Texas 76101
Attn: Librarian

General Motors Corporation
Allison Division
Indianapolis, Indiana 46206
Attn: Librarian

Hamilton Standard
Division of United Aircraft Corp.
Windsor Locks, Connecticut 06096
Attn: Librarian

Hughes Aircraft Company
Engineering Division
Culver City, California 90230
Attn: Librarian

Lawrence Radiation Lab.
Livermore, California 94550
Attn: Librarian

Lockheed Missiles and Space Div.
Lockheed Aircraft Corporation
Sunnyvale, California 90221
Attn: Librarian

The Martin Company
Nuclear Division
P.O. Box 5042
Baltimore, Maryland 21203
Attn: Librarian

Martin Marietta Corporation
Metals Technology Laboratory
Wheeling, Illinois 60090

Materials Research Corporation
Orangeburg, New York 10962
Attn: Librarian

McDonnel Aircraft
St. Louis, Missouri 63166
Attn: Librarian

MSA Research Corporation
Callery, Pennsylvania 16024
Attn: Librarian

National Research Corporation
70 Memorial Drive
Cambridge, Massachusetts 02142
Attn: Librarian

North American Rockwell
Los Angeles Division
Los Angeles, California 90009
Attn: Librarian

United Aircraft Corporation
Pratt & Whitney Aircraft Division
400 Main Street
East Hartford, Connecticut 06108
Attn: Librarian

Republic Aviation Corporation
Farmingdale, Long Island, New York 11735
Attn: Librarian

Sandia Corporation
P.O. Box 5800
Albuquerque, New Mexico 87116
Attn: Librarian

Sandia Corporation
P.O. Box 5800
Albuquerque, New Mexico 87116
Attn: Don Johnson

Solar
2200 Pacific Highway
San Diego, California 92112
Attn: Librarian

Southwest Research Institute
8500 Culebra Road
San Antonio, Texas 78220
Attn: Librarian

Superior Tube Company
Norristown, Pennsylvania 19404
Attn: L. Shaheen

Philco Corporation
Aeronutronics
Newport Beach, California 92663
Attn: Librarian

Report Distribution List - NAS 3-10610 - Topical (Continued)

General Electric Company
Nuclear Systems Program
Space Division
Cincinnati, Ohio 45215

General Electric Company
Evendale, Ohio 45215
Technical Information Center
Building 700, Mail Drop N-32

TRW Inc.
23555 Euclid Avenue
Cleveland, Ohio 44117
Attn: Librarian

Union Carbide Corporation
Materials Systems Division
1020 W. Park
Kokomo, Indiana 46901
Attn: Librarian

Union Carbide Corporation
Materials Systems Division
1020 W. Park
Kokomo, Indiana 46901
Attn: Technology Department

Wah Chang Corporation
Albany, Oregon 97321
Attn: Librarian

Westinghouse Electric Corporation
Astronuclear Laboratory
P.O. Box 10864
Pittsburgh, Pennsylvania 15236
Attn: R. W. Luckman

Westinghouse Electric Corporation
Astronuclear Laboratory
P.O. Box 10864
Pittsburgh, Pennsylvania 15236
Attn: G. G. Lessman

Westinghouse Electric Corporation
Astronuclear Laboratory
P.O. Box 10864
Pittsburgh, Pennsylvania 15236
Attn: D. R. Stoner

Westinghouse Electric Corporation
Astronuclear Laboratory
P.O. Box 10864
Pittsburgh, Pennsylvania 15236
Attn: Librarian

Whittaker Corporation
Nuclear Metals Division
West Concord, Massachusetts 01781
Attn: P. Lowenstein

Geoscience, Ltd.
410 S. Cedros Avenue
Solana Beach, California 92075
Attn: H. Poppendiek

NASA
Lewis Research Center
21000 Brookpark Road
Cleveland, Ohio 44135
Attn: N.T. Saunders, MS 105-1